Evaluation of Selected Finite-Difference and Finite-Volume Approaches to Rotational Shallow-Water Flow

Håvard H. Holm[1,3,*], André R. Brodtkorb[1,4], Göran Broström[2,5], Kai H. Christensen[2,6], and Martin L. Sætra[2,4]

[1] *SINTEF Digital, Mathematics & Cybernetics, P.O. Box 124 Blindern, NO-0314 Oslo, Norway.*
[2] *Norwegian Meteorological Institute, P.O. Box 43 Blindern, NO-0313 Oslo, Norway.*
[3] *Norwegian University of Science and Technology, Department of Mathematics, NO-7491 Trondheim, Norway.*
[4] *Oslo Metropolitan University, Department of Computer Science, P.O. Box 4 St. Olavs plass, NO-0130 Oslo, Norway.*
[5] *University of Gothenburg, Department of Marine Sciences, P.O. Box 461, SE-405 30 Göteborg, Sweden.*
[6] *University of Oslo, Department of Geosciences, P.O. Box 1047 Blindern, NO-0316 Oslo, Norway*

Abstract. The shallow-water equations in a rotating frame of reference are important for capturing geophysical flows in the ocean. In this paper, we examine and compare two traditional finite-difference schemes and two modern finite-volume schemes for simulating these equations. We evaluate how well they capture the relevant physics for problems such as storm surge and drift trajectory modelling, and the schemes are put through a set of six test cases. The results are presented in a systematic manner through several tables, and we compare the qualitative and quantitative performance from a cost-benefit perspective. Of the four schemes, one of the traditional finite-difference schemes performs best in cases dominated by geostrophic balance, and one of the modern finite-volume schemes is superior for capturing gravity-driven motion. The traditional finite-difference schemes are significantly faster computationally than the modern finite-volume schemes.

AMS subject classifications: 76U05, 86A05, 35L65, 65M08

Key words: Rotational shallow-water simulations, storm surge modelling, hyperbolic conservation laws, high-resolution finite-volume methods, test cases, verification.

*Corresponding author. *Email addresses:* Havard.Heitlo.Holm@sintef.no (H. H. Holm), Andre.Brodtkorb@sintef.no (A. R. Brodtkorb), Goran.Brostrom@marine.gu.se (G. Broström), kaihc@met.no (K. H. Christensen), martinls@met.no (M. L. Sætra)

First published in Communications in Computational Physics in Volume 27, Issue 4, published by Global Science Press.
DOI: https://dx.doi.org/10.4208/cicp.OA-2019-0033

1 Introduction

In this paper, we examine four different numerical schemes for the shallow-water equations in a rotating frame. These equations are important for a range of application areas, including simulation of the ocean and atmosphere. We focus on oceanographic simulations, in which the equations can capture the short-term ocean dynamics that are important for e.g., storm surge predictions. Our aim is to evaluate the suitability of the numerical schemes for use in an ensemble prediction system with data assimilation. One example is the propagation of long waves in an ocean basin sufficiently large so that the motion is constrained by geostrophy, and where we need to consider the effects of topography and nonlinearity, e.g. in the Barents Sea, which is fairly shallow but have large tidal range. We emphasize that we do not seek realistic solutions of the ocean dynamics for specific regions here, but rather aim to compare the various schemes using a range of parameters relevant for such dynamics.

In the early days of computational oceanography, finite-difference schemes were popular to simulate the rotational shallow-water equations. With increasing computational power, more complex physics, grids, and new discretization methods have appeared. Today's state-of-the-art ocean circulation models are sophisticated 3D simulations that capture a lot of the physical driving forces of the ocean currents, yet these models are computationally demanding and therefore allow only a limited number of ensemble members to be run in reasonable time.

We revisit two finite-difference schemes from early computational oceanography and compare these against two modern finite-volume schemes. One of our motivations for comparing finite-volume and finite-difference discretizations is that there has been recent developments in the finite-volume community for the rotating shallow-water equations, and we want to evaluate these from a cost-benefit perspective against well-known models.

The dominant force balance in the equations implies a nonzero current as a steady state, as the pressure gradient needs to be balanced by the Coriolis forces (so-called geostrophic balance). This is very different from problems in which the Earth's rotation can be ignored, where a typical steady state would imply zero velocities, often referred to as "lake-at-rest". This difference has important implications for the discretization of numerical schemes, and has been one of the driving factors in the development of modern high-resolution finite-volume methods which are well-balanced according to such steady-state solutions.

The four selected schemes in this work are all based on Cartesian grids, and are selected both because they capture the important geostrophic balance required for short-term predictions, and because they are very well suited for implementation on the GPU. Our long-term goal is to run large ensembles of such models, initialized and downscaled from operational 3D circulation models, on the GPU. These large ensembles can then be used on-demand to provide uncertainty estimates in predictions of storm surge or in drift trajectory modelling. The four numerical schemes we examine are:

FBL The Forward-Backward-Linear (FBL) finite-difference scheme on an Arakawa C grid [31] is based on a linearization of the shallow-water equations, and can therefore only represent the linear physics of ocean circulation. However, due to its simplicity it is very efficient and is therefore included to be evaluated from a cost-benefit perspective.

CTCS The Centered-in-Time Centered-in-Space (CTCS) scheme is a classic finite-difference leapfrog scheme on an Arakawa C grid. It is arguably one of the simplest numerical schemes used for geophysical flows, and is well-known and suited for geostrophically balanced flows. It is hence adequate as a reference to compare the finite-volume schemes against.

KP The high-resolution finite-volume Kurganov-Petrova scheme [23] has traditionally been used for modelling fast waves in non-rotating reference frames (e.g., dam break problems), and efficient implementations on heterogeneous platforms have been demonstrated [5]. In this work, we have added a naïve discretization of the Coriolis force, and the scheme illustrates the benefits and drawbacks of such an approach.

CDKLM The high-resolution finite-volume scheme introduced by Chertock et al. [6] is similar to the KP scheme, but it is specifically tailored to capture steady states which are in geostrophic balance. It represents a modern finite-volume scheme tailored to oceanographic applications.

We have evaluated these numerical schemes using a set of six test cases that contain important components of the transient barotropic ("fast", see Section 2) dynamics. The test cases are relevant for shelf seas or basin scale applications, and include both fast moving (Kelvin) and slow moving (Rossby) waves. The latter is particularly interesting since we obtain essentially the same wave phenomena from latitudinal variations in the Coriolis parameter compared with equivalent variations in topography. This provides a robust test of the higher-order schemes.

The rest of this paper is structured as follows. The remainder of this section mentions some relevant related work. Section 2 introduces the rotational shallow-water equations in an oceanography setting and describes the mathematical model from both the oceanographic and the finite volume perspective. Section 3 outlines the selected numerical schemes, followed by a detailed description of the test cases and results in Section 4. Finally, the paper is summarized in Section 5. As we anticipate some readers may not be familiar with all concepts of geophysical fluid dynamics, we provide some underlying theory in A.

The software used herein has been designed to be suitable for a high-performance ensemble prediction system with non-linear data assimilation. The test cases we use are comprehensively described and tailored to be reproducible for other researchers using the current simulation framework or other codes, and the numerical schemes are imple-

mented on the GPU for efficiency. Both the full source code and relevant test case setups are available as supplementary material.

Related work

There has been a substantial effort in designing numerical schemes for the shallow-water equations using various approximation methods (e.g., finite volume [25, 44], finite difference [35, 40], lattice Boltzmann [48], and discontinuous Galerkin [7, 33]). The finite-volume community has recently shown an interest in rotational shallow-water flows (i.e., flows under the influence of the Coriolis force). This has led to the development of schemes that is well-balanced with respect to the geostrophic balance [6], and not only with respect to the lake-at-rest solution [34]. Furthermore, some of these higher-order numerical schemes are particularly suitable for implementation on massively data parallel architectures like the GPU [4, 5, 10, 24, 26]. Some mature software packages, such as Clawpack [27], also have GPU implementations of some finite-volume schemes [37], and several commercial packages, such as TUFLOW [22] and MIKE [32], have GPU support.

An implementation of any numerical scheme should be verified against appropriate analytical solutions, or validated against specially designed test cases or real-world data. For the non-rotating shallow-water equations, there are several well-established reference solutions for specific physical phenomena, see e.g., [11–13, 17, 18, 20, 43, 46]. In the case of rotating shallow-water flow, a notable test set is described by Williamson et al. [47], and includes both analytic and high-resolution reference solutions to seven test cases defined on the sphere. The test set has also been suggested extended by Galewsky et al. [14]. Comblen et al. [8] used a set of eight test cases for evaluating five different pairs of finite-element methods for solving the rotational shallow-water equations on a flat two-dimensional domain. A similar approach with six test cases was used by Tumolo et al. [45] to evaluate their discontinuous Galerkin method for solving the same problem.

2 The Rotating Shallow-Water Equations

The shallow-water equations describe flows in ”shallow” water, meaning that the horizontal scales of the problem are much larger than the water depth, and are here considered on a rotating domain. The equations can describe important physical processes found in the ocean, such as tide propagation, storm surge, and wave phenomena such as inertial oscillations, Kelvin waves, and Rossby waves induced by changes in bottom topography or in the Coriolis force. It is commonly assumed that the pressure distribution is hydrostatic and that the vertical acceleration can be neglected. The pressure at any specific point is then simply a function of the water density and the height of the water column above it. For some physical processes, such as large-amplitude or higher-mode internal waves, the hydrostatic approximation cannot be used, but in general the approximations involved do not lead to significant errors for barotropic flows. Strictly speaking,

barotropic motion is characterized by coincidental surfaces of constant pressure and constant density, but can be thought of as motion with negligible vertical shear. The opposite case gives rise to baroclinic motion, and examples here include internal waves and instabilities that can develop into ocean eddies. In general, barotropic signals propagate much faster than baroclinic signals, which is a challenge in numerical ocean circulation models, because the temporal resolution required for numerical stability can differ by one or two orders of magnitude. This problem is typically overcome by using so-called mode splitting, with different time-step sizes for the integration of the barotropic and baroclinic components, respectively (e.g., [41]).

The shallow-water equations are often expressed differently by those working with hyperbolic conservation laws and those working with ocean modelling, even though the starting point in both cases is the Navier-Stokes equations. Both communities use equations in flux form that are essentially hyperbolic, but in the oceanographic community it is customary to keep all forcing terms separate from the conservation of momentum. On the other hand, the community working with hyperbolic conservation laws typically include parts of the forces due to pressure gradients in the flux term, and this results in a different set of forcing terms in the equations.

In this section, both formulations of the shallow-water equations are presented, and we show how they are equivalent. For simplicity, viscous terms due to surface and bottom stresses, and variations in the atmospheric forcing are ignored. Both formulations are essentially based on vertical integration of the governing equations, with kinematic boundary conditions prescribing no flow normal to fixed boundaries and a moving free surface.

2.1 Classical Formulation as Hyperbolic Conservation Laws

In the context of hyperbolic conservation laws (e.g., [25]), the shallow-water equations are derived by considering conservation of mass and momentum. The starting point is the Navier-Stokes equations, which are depth integrated under the assumptions mentioned above. Among those working with finite-volume methods for hyperbolic conservation laws, the shallow-water equations are often written as

$$\begin{bmatrix} h \\ hu \\ hv \end{bmatrix}_t + \begin{bmatrix} hu \\ hu^2+\frac{1}{2}gh^2 \\ huv \end{bmatrix}_x + \begin{bmatrix} hv \\ huv \\ hv^2+\frac{1}{2}gh^2 \end{bmatrix}_y = \begin{bmatrix} 0 \\ fhv \\ -fhu \end{bmatrix} + \begin{bmatrix} 0 \\ -ghB_x \\ -ghB_y \end{bmatrix}. \tag{2.1}$$

Here, h is water depth, and u and v denote water velocity in x- and y-direction, respectively. The conserved variables hu and hv represent the volume transport, also referred to as discharge or momentum. The source terms on the right-hand-side represent the Coriolis force caused by the rotation of the Earth and acceleration due to gravity over a varying bathymetry. The bathymetry is described by $B(x,y)$ as elevation above a reference level.

In the present applications, water depth h can often be in the range of 1000 meters, while the change in surface elevation across time-steps is typically only a few centimeters,

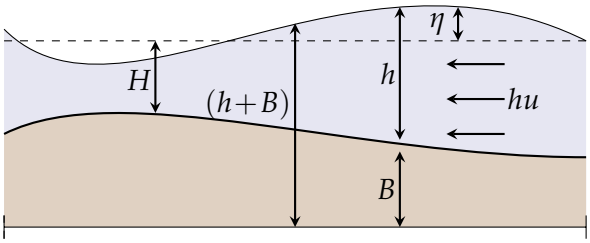

Figure 1: Relationship between variables h, H, η, hu and B, appearing in the two formulations of the shallow-water equations, here shown in one dimension.

resulting in five orders of magnitude difference. For better numerical representation, we can rewrite the problem in terms of the deviation η from equilibrium water depth. Denoting equilibrium water depth as H, so that $h=\eta+H$, (2.1) becomes

$$\begin{bmatrix}\eta\\ hu\\ hv\end{bmatrix}_t+\begin{bmatrix}hu\\ \frac{(hu)^2}{H+\eta}+\frac{1}{2}g(H+\eta)^2\\ \frac{(hu)(hv)}{H+\eta}\end{bmatrix}_x+\begin{bmatrix}hv\\ \frac{(hu)(hv)}{H+\eta}\\ \frac{(hv)^2}{H+\eta}+\frac{1}{2}g(H+\eta)^2\end{bmatrix}_y=\begin{bmatrix}0\\ fhv\\ -fhu\end{bmatrix}+\begin{bmatrix}0\\ g(H+\eta)H_x\\ g(H+\eta)H_y\end{bmatrix}. \quad (2.2)$$

Here, we have used the fact that H is independent of time and that the slope of H and B have opposite signs. Relationships between all the introduced variables are shown in Figure 1 for the one-dimensional case.

By denoting the vector of conserved varibles as $\boldsymbol{q}=[\eta,hu,hv]^T$, we can write (2.2) in vector form as

$$\boldsymbol{q}_t+F(\boldsymbol{q})_x+G(\boldsymbol{q})_y=S_f(\boldsymbol{q})+S_H(\boldsymbol{q},\nabla H), \quad (2.3)$$

in which F and G represent fluxes along the abscissa and ordinate, respectively, and S_f and S_H are the Coriolis and bed slope source terms, respectively.

2.2 Classical Formulation in Physical Oceanography

Within the physical oceanography community, the shallow-water equations are typically derived by using the continuity equation along with the Navier-Stokes equations [35]. After vertical integration of the governing equations and application of the kinematic boundary conditions, we end up with the following form for the shallow-water equations:

$$\eta_t+\nabla_H\cdot\boldsymbol{U}=0, \quad (2.4)$$

$$\boldsymbol{U}_t+\nabla_H\cdot\left(\frac{\boldsymbol{U}\boldsymbol{U}}{h}\right)=-gh\nabla_H\eta-f\boldsymbol{k}\times\boldsymbol{U}+A\nabla_H^2\boldsymbol{U}. \quad (2.5)$$

The horizontal divergence is denoted $\nabla_H = [\boldsymbol{i}\frac{\partial}{\partial x}, \boldsymbol{j}\frac{\partial}{\partial y}, 0]^T$. Here, $\boldsymbol{i}$ and $\boldsymbol{j}$ are the horizontal unit vectors, whereas $\boldsymbol{k}$ is the vertical unit vector. Further, the vector $\boldsymbol{U}$ is the depth integrated volume transport, $\boldsymbol{U} = [hu, hv, 0]^T$. The final term represents an explicit parametrization of a diffusive process that is sometimes used to avoid nonlinear numerical instabilities when the equations are solved with e.g., the classical leapfrog finite-difference method considered herein. The constant A is referred to as the eddy viscocity parameter. In (2.4) and (2.5), vertical shear stresses caused by bottom friction and wind drag on the surface are ignored.

By examining the two different formulations of the shallow-water equations, we observe that (2.4) is equal to the first row of (2.2), since

$$\eta_t + \nabla_H \cdot \boldsymbol{U} = \eta_t + (hu)_x + (hv)_y = 0.$$

A closer look at the second nonlinear term of (2.5) reveals that

$$\nabla_H \cdot \left(\frac{\boldsymbol{U}\boldsymbol{U}}{h}\right) = \nabla_H \cdot \frac{1}{h}\begin{bmatrix} (hu)^2 & (hu)(hv) & 0 \\ (hu)(hv) & (hv)^2 & 0 \\ 0 & 0 & 0 \end{bmatrix} = \begin{bmatrix} (hu^2)_x + (huv)_y \\ (huv)_x + (hv^2)_y \\ 0 \end{bmatrix},$$

in which we can recognize the non-gravity driven flux terms from the second and third row of (2.1). Next, we consider the gravity induced flux terms and the bathymetry source term in x-direction from (2.1), moving the source term to the left-hand side. By using $h = \eta + H$ and the fact that $\nabla_H H = -\nabla_H B$, these two terms can be written as

$$\left(\frac{1}{2}gh\right)_x + ghB_x = gh(\eta_x + H_x) + ghB_x = gh\eta_x,$$

which we recognise on the right-hand side of (2.5). The same manipulation applies in y-direction. If we ignore the eddy viscosity term, and since

$$f\boldsymbol{k} \times \boldsymbol{U} = [-f(hu), f(hv), 0]^T,$$

we see that the first and second row of (2.5) correspond to the second and third row of (2.1). The third row of (2.5) represents the vertical momentum, which is zero on both sides of the equation.

The eddy viscosity $A\nabla_H^2 \boldsymbol{U}$ in (2.5) is not represented in (2.1). This is because it is related to stability issues in the leapfrog finite-difference scheme [1], an issue not present with the finite-volume schemes for which the formulation (2.1) is used.

3 Numerical Schemes

In the following, we give an overview of four different numerical schemes for solving the rotational shallow-water equations. The first two schemes are finite-difference methods,

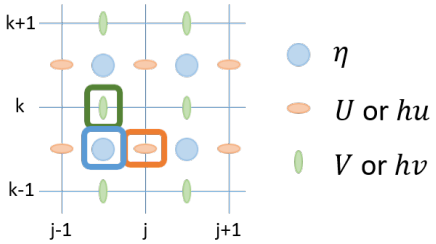

Figure 2: The discretized conserved variables on a staggered lattice C grid.

and the latter two are high-resolution finite-volume methods, in which the term high-resolution refers to the schemes' ability to accurately capture discontinuities. At the end of this section we describe three boundary conditions, and discuss the main differences between the selected schemes.

3.1 Forward-Backward Linear Scheme

The first scheme is the Forward-Backward Linear (FBL) finite-difference scheme, first presented by Sielecki [42]. It considers η, $U=hu$, and $V=hv$, in which U and V are used for the volume transport to provide a more compact notation. The scheme is based on the linearized equations

$$\begin{aligned} \eta_t &= -U_x - V_y, \\ U_t - fV &= -gH\eta_x, \\ V_t + fU &= -gH\eta_y, \end{aligned} \tag{3.1}$$

arising from scalar linearization of (2.4) and (2.5). The name of the scheme reflects the first-order discretization used in time, while second-order central differences are applied in space [39].

To write out a finite-difference method for (3.1), consider a regular Cartesian discretization on a rectangular domain. Let Δx and Δy be the distance between each point in the grid, and define $x_j = j\Delta x$ for $j=0,\ldots,N_x$, and $y_k = k\Delta y$ for $k=0,\ldots,N_y$. The variables η, U, and V are defined according to a lattice C grid, as defined by Mesinger and Arakawa [31] and shown in Figure 2. The discretized variables then become

$$\begin{aligned} \eta^n_{j,k} &= \eta(x_j - \frac{1}{2}\Delta x, y_k - \frac{1}{2}\Delta y, t_n), \\ U^n_{j,k} &= U(x_j, y_k - \frac{1}{2}\Delta y, t_n), \\ V^n_{j,k} &= V(x_j - \frac{1}{2}\Delta x, y_k, t_n), \end{aligned} \tag{3.2}$$

in which t_n is time-step n.

The finite-difference method uses an asymmetric update in time, in which each of the variables are updated based on the most recent available state of the others. The FBL scheme is then given as

$$\begin{aligned}
U_{j,k}^{n+1} &= U_{j,k}^{n} + \Delta t \overline{fV}_{j,k}^{n} + \frac{\Delta t}{2\Delta x} g\left(H_{j+1,k} + H_{j,k}\right)\left(\eta_{j+1,k}^{n} - \eta_{j,k}^{n}\right), \\
V_{j,k}^{n+1} &= V_{j,k}^{n} - \Delta t \overline{fU}_{j,k}^{n+1} + \frac{\Delta t}{2\Delta x} g\left(H_{j,k+1} + H_{j,k}\right)\left(\eta_{j,k+1}^{n} - \eta_{j,k}^{n}\right), \\
\eta_{j,k}^{n+1} &= \eta_{j,k}^{n} - \frac{\Delta t}{\Delta x}\left(U_{j,k}^{n+1} - U_{j-1,k}^{n+1}\right) - \frac{\Delta t}{\Delta x}\left(V_{j,k}^{n+1} - V_{j,k-1}^{n+1}\right),
\end{aligned} \tag{3.3}$$

in which

$$\begin{aligned}
\overline{fU}_{j,k}^{n} &= \frac{1}{4}\left(f_{k-\frac{1}{2}} U_{j,k}^{n} + f_{k-\frac{1}{2}} U_{j-1,k}^{n} + f_{k+\frac{1}{2}} U_{j-1,k+1}^{n} + f_{k+\frac{1}{2}} U_{j,k+1}^{n}\right), \\
\overline{fV}_{j,k}^{n} &= \frac{1}{4}\left(f_{k} V_{j,k}^{n} + f_{k} V_{j+1,k}^{n} + f_{k+1} V_{j+1,k-1}^{n} + f_{k+1} V_{j,k-1}^{n}\right).
\end{aligned} \tag{3.4}$$

Since the Coriolis force varies with the latitude only, the discrete values of the Coriolis force is denoted as $f_k = f(y_k)$. The grid values required for each of these stencils are shown in Figure 3.

The scheme requires that initial conditions for η, U, and V are given at $t = t_0$, as well as boundary conditions for U at $x = 0$ and $x = N_x \Delta x$, and for V at $y = 0$ and $y = N_y \Delta y$ for $t \geq t_0$. In the ocean the fastest signals are due to barotropic shallow-water waves, propagating with speed $|u| + \sqrt{gH_{max}}$, in which H_{max} is the maximum equilibrium water depth. Since the fluid velocities $|u|$ are usually at least one order of magnitude smaller than the gravitational term, the relevant Courant-Friedrich-Levy (CFL) condition in for FBL becomes

$$\Delta t \leq \frac{\min(\Delta x, \Delta y)}{\sqrt{2gH_{max}}}. \tag{3.5}$$

3.2 Centered-in-Time, Centered-in-Space Scheme

The centered-in-time, centered-in-space (CTCS) finite-difference scheme discretizes the full nonlinear equations given in (2.4) and (2.5), using the same staggered grid as FBL. It is a leapfrog scheme, and can be summarized by the stencils

$$\begin{aligned}
\eta_{j,k}^{n+1} &= \eta_{j,k}^{n-1} - \frac{2\Delta t}{\Delta x}\left(U_{j,k}^{n} - U_{j-1,k}^{n}\right) - \frac{2\Delta t}{\Delta y}\left(V_{j,k}^{n} - V_{j,k-1}^{n}\right), \\
U_{j,k}^{n+1} &= \frac{1}{B_{j,k}^{x}}\left[U_{j,k}^{n-1} + 2\Delta t\left(\overline{fV}_{j,k}^{n} + \frac{1}{\Delta x} N_{j,k}^{x} + \frac{1}{\Delta x} P_{j,k}^{x} + AE_{j,k}^{x}\right)\right], \\
V_{j,k}^{n+1} &= \frac{1}{B_{j,k}^{y}}\left[V_{j,k}^{n-1} + 2\Delta t\left(-\overline{fU}_{j,k}^{n} + \frac{1}{\Delta y} N_{j,k}^{y} + \frac{1}{\Delta y} P_{j,k}^{y} + AE_{j,k}^{y}\right)\right].
\end{aligned} \tag{3.6}$$

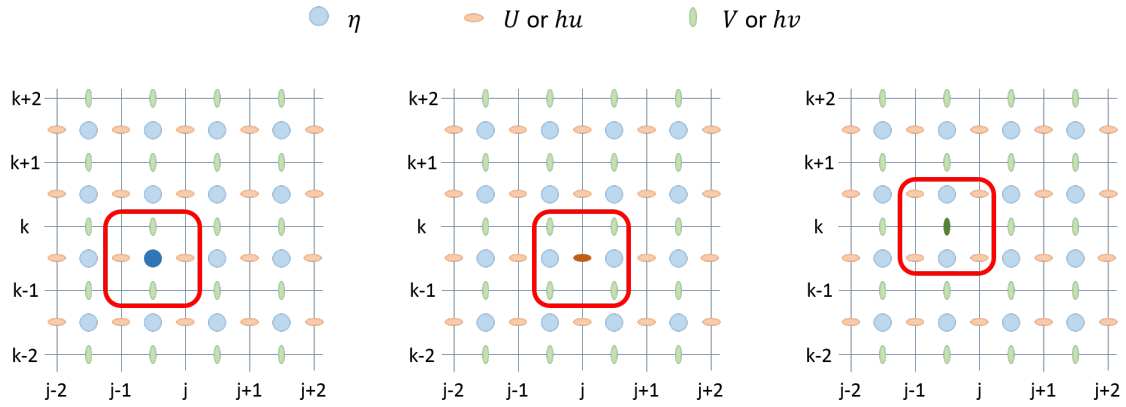

(a) Stencil for $\eta_{j,k}$. (b) Stencil for $U_{j,k}$. (c) Stencil for $V_{j,k}$.

Figure 3: Finite-difference stencils for the FBL scheme. Blue circles represent η, while orange horizontal ellipses and green vertical ellipses represent U and V, respectively. Note that the water depth H is collocated with η.

The factors $\overline{fU}$ and $\overline{fV}$ are the same as for the FBL scheme, given in (3.4), while the N and P terms handle the momentum fluxes and gravity pressure terms, respectively. The terms E and B are all used to handle the eddy viscosity term, and the interested reader can find details of the full scheme in Røed [39]. Unlike the FBL scheme, CTCS is symmetric in time and space, as all three variables are updated independently for each time-step, allowing all three stencils to be computed in parallel within each time-step.

The complete set of grid values required for each of these stencils is shown in Figure 4. In addition to the boundary conditions required for the FBL scheme, it is also necessary to define values for η and U at $y=-\frac{1}{2}\Delta y$ and $y=(N_y+\frac{1}{2})\Delta y$, and correspondingly for η and V at $x=-\frac{1}{2}\Delta x$ and $x=(N_x+\frac{1}{2})\Delta x$. Since the stencil also includes terms from $t=t_{n+1}$, initial conditions for both t_0 and t_{-1} are required.

The stability of the CTCS scheme is restricted under half the CFL criterion (3.5) as the FBL scheme [40]. Additionally, the CTCS scheme is known to suffer under nonlinear instability [36,38,40]. The nonlinearity of the equations allows energy to be redistributed between waves of different wave lengths, causing energy to be transferred from long waves to shorter ones. As the solution on the discrete grid is unable to represent waves with wave lengths shorter than $2\Delta x$, waves with wave lengths between $2\Delta x$ and $4\Delta x$ tend to increase in amplitude, and eventually lead to unstable solutions. The eddy viscosity term, controlled empirically through the A parameter, introduces artificial diffusion into the scheme, damping the shorter waves and avoiding the solution to be dominated by strong short waves.

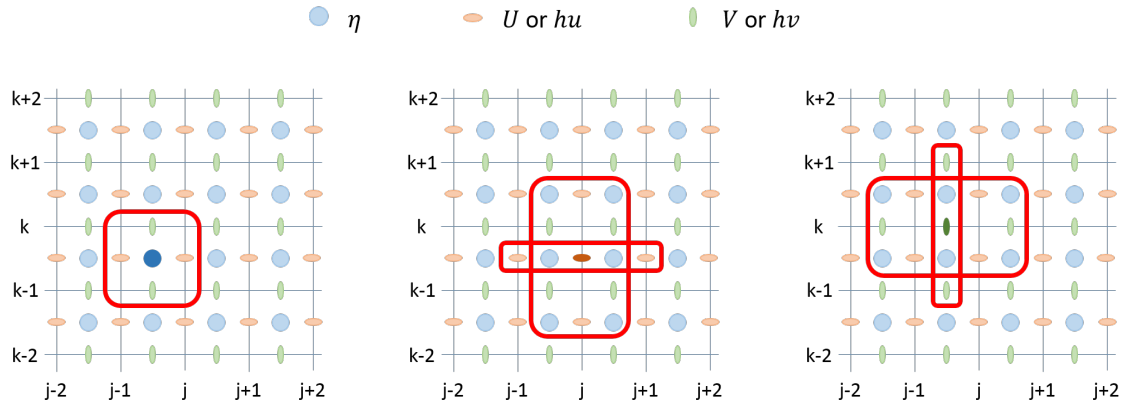

(a) Stencil for $\eta_{j,k}$. (b) Stencil for $U_{j,k}$. (c) Stencil for $V_{j,k}$.

Figure 4: Finite-difference stencils for the CTCS scheme. Blue circles represent η, while orange horizontal ellipses and green vertical ellipses represent U and V, respectively.

3.3 Kurganov-Petrova Scheme

The Kurganov-Petrova 2007 (KP) scheme [23] is a high-resolution finite-volume scheme [25], and is based on the full nonlinear equations (2.2). The flux terms are computed by a well-balanced, positivity-preserving, central-upwind method. This means that the flux balances the bathymetry source terms so that lake-at-rest solutions are preserved, even in the presence of discontinuous bathymetry. The scheme ensures that the water depth always is non-negative, which is important at wet-dry interfaces. The scheme has built-in numerical diffusion, and hence does not have the same problem with nonlinear instabilities due to build-up of energy at the smallest spatial scales, as is the case with CTCS.

KP can be written as

$$\begin{aligned}\frac{d\boldsymbol{Q}_{j,k}}{dt} &= S_f(\boldsymbol{Q}_{j,k}) + S_H(\boldsymbol{Q}_{j,k}, \nabla H) - \left[F(\boldsymbol{Q}_{j+1/2,k}) - F(\boldsymbol{Q}_{j-1/2,k})\right] \\ &\quad - \left[G(\boldsymbol{Q}_{j,k+1/2}) - G(\boldsymbol{Q}_{j,k-1/2})\right], \\ &:= R(\boldsymbol{Q})_{j,k}.\end{aligned} \tag{3.7}$$

Here $\boldsymbol{Q}_{j,k}$ is the vector of conserved variables averaged over the grid cell centered at $((j+\frac{1}{2})\Delta x, (k+\frac{1}{2})\Delta y)$, for $j=0,\ldots,N_x-1$ and $k=0,\ldots,N_y-1$. Further, S_f and S_H are discretized Coriolis and bed slope source terms, respectively, and F and G represent numerical flux functions.

The scheme consists of the following steps: From the averaged cell values, a piecewise bilinear polynomial of $\boldsymbol{Q}$ is *reconstructed* by using the generalized minmod limiter. The slope allows us to evaluate $\boldsymbol{Q}$ at each side of every face, and the central-upwind numerical flux function is used to compute F and G. The solution is then *evolved* in time, by

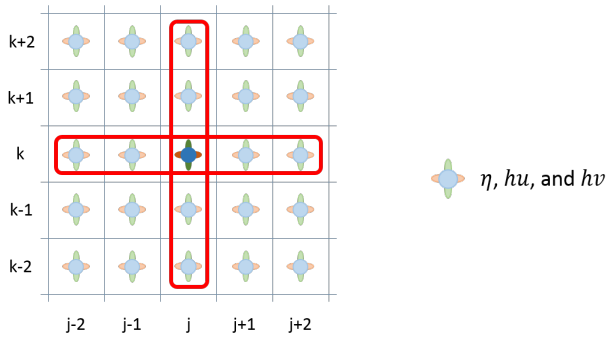

Figure 5: Stencil for the KP and CDKLM schemes. Blue circles represent η, while orange horizontal ellipses and green vertical ellipses represent U and V, respectively.

using a second-order, strong stability preserving Runge–Kutta method [16]:

$$\begin{aligned} \boldsymbol{Q}^*_{j,k} &= \boldsymbol{Q}^n_{j,k} + \Delta t R(\boldsymbol{Q}^n)_{j,k}, \\ \boldsymbol{Q}^{n+1}_{j,k} &= \tfrac{1}{2}\boldsymbol{Q}^n_{j,k} + \tfrac{1}{2}\left[\boldsymbol{Q}^*_{j,k} + \Delta t R(\boldsymbol{Q}^*)_{j,k}\right]. \end{aligned} \tag{3.8}$$

Here, Δt, is restricted by a CFL-condition which ensures that disturbances travel at most one quarter of a grid cell per time-step,

$$\Delta t \leq \frac{1}{4}\min\left\{ \frac{\Delta x}{\max_\Omega \left|u \pm \sqrt{g(H+\eta)}\right|}, \frac{\Delta y}{\max_\Omega \left|v \pm \sqrt{g(H+\eta)}\right|} \right\}. \tag{3.9}$$

The results from (3.8) are again *averaged* cell values at time t_{n+1}. In general, this is called a REA-algorithm [25], named after the steps reconstruct, evolve, and average. The KP scheme was originally designed to solve the non-rotating shallow-water equations. It is therefore worth noting that the discretization of the Coriolis source term here is made naïvely, as

$$S_f(\boldsymbol{Q}_{j,k}) = [0, f(hv)_{j,k}, -f(hu)_{j,k}]^T.$$

Further details can be found in Kurganov and Petrova [23], and a GPU implementation is presented by Brodtkorb et al. [5].

The stencil for the KP scheme is shown in Figure 5. Note that no variables are defined on the exact domain boundary. Instead, boundary conditions on all three conserved variables are required to be defined in two layers of ghost cells surrounding the computational domain. To start the simulation, initial conditions must be defined at $t = t_0$.

3.4 The CDKLM Scheme

The fourth scheme considered in this paper is a novel high-resolution finite-volume scheme, presented by Chertock et al. [6] (CDKLM). It is similar to the KP scheme with re-

spect to the numerical formulation of flux terms, and is based on the same semi-discrete form as in (3.7).

Whereas KP is designed to be well-balanced with respect to the steady-state, lake-at-rest solution, the CDKLM scheme aims to be well-balanced with respect to the steady-state solution given by the geostrophic balance, from (A.3). This is achieved by introducing reconstruction variables $\boldsymbol{R} = [u, v, K, L]^T$. Here, K and L are Coriolis potentials given by

$$K := g(\eta - f_v), \qquad L := g(\eta + f_u), \tag{3.10}$$

in which $[f_u, f_v]^T$ are the primitives of the Coriolis force, defined through their derivatives,

$$(f_v)_x := \frac{f}{g} v, \qquad (f_u)_y := \frac{f}{g} u. \tag{3.11}$$

The CDKLM scheme follows a similar REA-algorithm as the KP scheme, but instead of basing the reconstruction on $\boldsymbol{Q}$, the scheme reconstructs a piecewise bilinear polynomial of $\boldsymbol{R}$. Piecewise reconstructions of η, u, and v are then obtained from the reconstructed $\boldsymbol{R}$, and used to evaluate central-upwind numerical fluxes. These are used to update $\boldsymbol{Q}$ in time through a sufficiently accurate total-variation-diminishing Runge–Kutta method.

In summary, the CDKLM scheme uses the same numerical flux function and reconstruction methodology as the KP scheme, but takes the Coriolis forces into account for properly representing known steady-state solutions. Both these schemes are considered to investigate whether the more complex handling of the Coriolis forces pays of in terms of better simulation results. The shape of the stencil for the CDKLM scheme is similar to the one for KP, shown in Figure 5. Because of this, the requirement to initial and boundary conditions are the same for the two schemes, as well.

3.5 Boundary Conditions

All schemes in the simulation framework support three different boundary conditions: reflective wall-, periodic-, and open-boundary conditions. All three are implemented by modifying the solution in the ghost cell region, which constitute of a band of cells or grid points encircling the original computational domain. As a minimum, the ghost cell region is required to be large enough so that the outermost grid points in the original domain can be computed with the chosen stencil. In general, boundary conditions are more conveniently implemented using staggered grids where the grid points for the velocity components and the pressure (or free surface) do not coincide. Staggered grids are also very useful to maintain the geostrophic balance, so that difference schemes for the components of the pressure gradient are centered at the relevant (u, v) velocity grid points.

The reflective wall boundary condition is designed to preserve mass and momentum within the original domain. This is achieved by creating an ingoing momentum in the

ghost region equal to the outgoing momentum in the interior. Let x^W be the location of the western boundary, so that $x = x^W + \hat{x}$ is in the interior of the domain for some $\hat{x} > 0$. Reflective wall boundary conditions are obtained by setting the values in the ghost region according to

$$\begin{aligned} \eta(x^W - \hat{x}) &= \eta(x^W + \hat{x}), \\ hu(x^W - \hat{x}) &= -hu(x^W + \hat{x}), \\ hv(x^W - \hat{x}) &= hv(x^W + \hat{x}). \end{aligned} \tag{3.12}$$

Note that the condition on hu implies that $hu(x^W) = 0$, so that no water is allowed to leave the domain. The same principle applies in the y-direction.

Periodic boundary conditions make flow reaching one boundary reappear on the opposite boundary. Let ϕ be any of the conserved variables, and let x^W and x^E be the location of the western and eastern boundary, respectively. Periodic boundary conditions are then defined as

$$\phi(x^W - \hat{x}) = \phi(x^E - \hat{x}), \tag{3.13}$$

for $\hat{x} > 0$, so that $x^W - \hat{x}$ is in the ghost region. Note that for staggered grids, discharge on the boundary needs to be computed by the stencil, expanding the computational domain with one extra row and column for v and u, respectively.

Regional ocean circulation models that cover limited areas require open boundary conditions in which external solutions can be imposed in such a way that external signals can propagate freely into the model domain and signals generated in the interior can propagate freely out of the domain [28]. To maintain the explicit and parallel structure of the simulation code, a flow relaxation scheme [9,29] is used. Let ψ^{ext} be the exterior solution far away from the interior domain. Define a ghost cell region consisting of N_G ghost cells, where N_G is larger than required by the shape of the numerical stencil. At each time-step, the stencil is applied to all cells having a sufficient number of neighbouring cells. The flow relaxation scheme relaxes the obtained solution in all ghost cells towards ψ^{ext},

$$\psi = (1-\alpha)\psi^* + \alpha\psi^{ext}. \tag{3.14}$$

Here, ψ^* is the solution from the numerical stencil, and α is a relaxation factor, so that $\alpha = 0$ at the boundary and $\alpha = 1$ in the outermost ghost cell. In this paper, the size of the ghost cell region is chosen to be $N_G = 10$ for all schemes, along with relaxation parameter

$$\alpha = 1 - \tanh\left(\frac{1-i}{3}\right), \tag{3.15}$$

for $i = 0,...,N_G - 1$.

3.6 Discussion

Table 1 gives a structured comparison of the four numerical schemes discussed above. The scheme that stands out the most is FBL, as it only solves the linearized equations,

Table 1: Comparison of properties of the four numerical schemes. The ghost cell region corresponds to how many rows of ghost cells for η you need to implement wall boundary conditions. The initial conditions row shows that CTCS needs the conserved variables for two time-steps.

	Numerical Scheme			
	FBL	**CTCS**	**KP**	**CDKLM**
Underlying equation	Linearized	Nonlinear	Nonlinear	Nonlinear
Coriolis discretization	Intrinsic	Intrinsic	Naïve addition	Intrinsic
Conservative	Yes	Yes	Yes	Yes
Discretization method	Finite difference	Finite difference	Finite Volume	Finite Volume
Grid	Arakawa C	Arakawa C	Arakawa A	Arakawa A
Order in space	2	2	2	2
Order in time	1	2	2	2
Ghost cell region	0	1	2	2
Initial conditions	1 (t_0)	2 (t_0,t_{-1})	1 (t_0)	1 (t_0)
CFL-condition relative to $\Delta x/c_0$	$1/\sqrt{2}$	$1/(2\sqrt{2})$	$1/4$	$1/4$
Relative numerical complexity	Simple	Fairly simple	Fairly complex	Complex

but it is still of interest due to its simplicity, and thereby its computational efficiency. The KP scheme is also notably different from the others, with its naïve discretization of the Coriolis forces. It is included in this study as it is interesting to investigate the differences between a scheme that is well-balanced with respect to lake-at-rest (KP), and a slightly more computational intensive scheme that is also well-balanced with respect to the geostrophic balance (CDKLM). All three nonlinear schemes are of second order in both time and space, while FBL is only first order in time.

On the practical side, there is a difference in the data dependency for the four schemes. We see that the finite-difference schemes have a smaller ghost cell region than the finite-volume schemes, and a consequence of this is that the boundary conditions are easier to implement for CTCS and FBL compared to for KP and CDKLM. Also, since the finite-difference schemes use an Arakawa C grid, it is easier to prescribe the momentum on the boundary than for the finite volume schemes which use an A grid. On the other hand, CTCS requires the state of the two previous time-steps in order to evolve, whereas the other three schemes require only one. A final advantage for the finite-difference schemes is that they allow for a larger time-step compared to the finite-volume schemes.

4 Test Cases and Results

In this section we evaluate the quality and behavior of the four numerical schemes described in Section 3 through a set of six test cases. The test cases focus on the intrinsic dynamics of shallow-water flows in a rotating reference frame, and we ignore the impact of atmospheric pressure, and friction caused by bed and wind shear stresses. It should be noted that although we study barotropic dynamics here, the equations are formally identical to the ones in so-called 1.5-layer models for a well mixed upper ocean layer above a deep ocean layer at rest [40]. A 1.5-layer model setup would in some cases provide for more geophysically relevant examples, e.g. Cases B and C, which in their present implementation have unrealistically large domains. We begin with non-rotating properties of the schemes in Case A, before we study the transient development arising from an initial disturbance in the sea surface elevation, investigating the so-called geostrophic (or Rossby) adjustment problem [2] in Cases B and C. We then look at Kelvin waves in Case D, in which fast moving shallow-water waves are trapped along the coast by the Coriolis force. The final two test cases, E and F, focus on Rossby waves caused by the dynamics in the potential vorticity, driven by variation in the Coriolis force and in the bathymetry, respectively. The physics behind the oceanographic test cases are described in more detail in A, but the essential points are summarized for each case for convenience.

4.1 Case A: Traditional Non-Rotating Shallow-Water Benchmarks

Our first benchmark case is described in SWASHES [11] and is a classical dam break case for non-rotational physics. The first part is ”lake-at-rest with an immersed bump” [11, Sec. 3.1.1], which validates that the numerical scheme is able to preserve a calm lake on

top of a non-constant bathymetry without any initial momentum. All four schemes pass this test.

The second part is a one-dimensional "dam break on a wet domain without friction" [11, Sec. 4.1.1], which validates the scheme's ability to capture shocks. The initial conditions consist of a step function in η with zero momentum, shown along with the simulation results in Figure 6. The analytic solutions [11] are given as black solid lines in the plot. This test case clearly shows that the finite-volume schemes are able to capture the shock with high precision, whereas the finite-difference schemes fail. The FBL scheme results in unstable oscillations, while CTCS gives various incorrect results for different choices for the eddy viscosity parameter A. High values for A gives a solution that resembles the initial state, and very low values for A results in unstable solutions. This is expected, given that FBL and CTCS with $A=0$ have no numerical diffusion, causing the schemes to break down in the presence of shock solutions. KP and CDKLM, on the other hand, have built-in numerical diffusion in their numerical fluxes, and are designed to capture discontinuities. Oceanographers are often not too concerned with shock solutions, as these are not part of the most important physics of oceanography, and this test illustrates that the finite difference schemes considered here are not designed with shocks in mind.

4.2 Case B: Rossby Adjustment

In this test case, and in Case C, we look at Rossby adjustment, a smooth dam break problem with rotation, in which an initial surface elevation in a limited area adjusts itself under gravity towards equilibrium. The case is designed to trigger a gravitational wave moving radially outwards from the center, similar to a radial dam break. Due to the rotation, parts of the fluid will become trapped within a length scale of the Rossby radius $L_R = c/f$ from the initial disturbance. Here, $c = \sqrt{gH}$ is the phase speed of free gravitational waves, and the basic balance will be the geostrophic solutions (A.3). In this case, f is considered to be constant, whereas variations in rotation and topography will be considered in cases E and F.

The Rossby adjustment problem investigates a scheme's ability to obtain and preserve steady-state solutions given by the geostrophic balance (A.3). We have a constant bathymetry, $H(x,y) = H_0$, and the initial state of the surface is formed as a bump,

$$\eta(x,y,t_0) = \frac{1}{2}\eta_0 \left[1 + \tanh\left(\frac{-\sqrt{(x-x_0)^2 + (y-y_0)^2} + D}{L} \right) \right], \tag{4.1}$$

in which D, L, and η_0 are related to the width, steepness, and maximum height of the bump, respectively. The center of the bump is positioned at (x_0, y_0), and the initial momentum is zero,

$$hu(x,y,t_0) = hv(x,y,t_0) = 0. \tag{4.2}$$

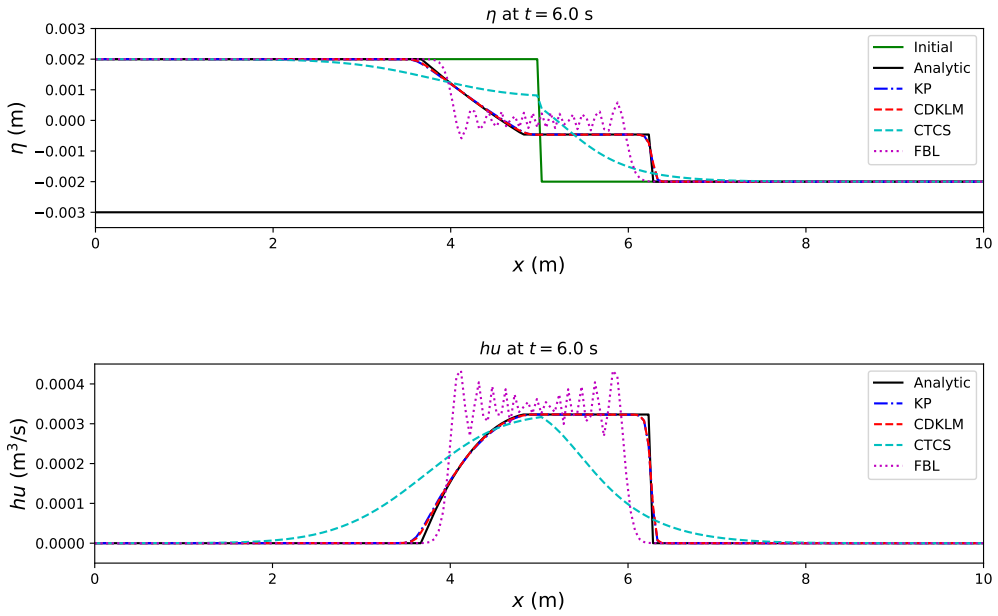

Figure 6: Case A: SWASHES test case 4.1.1 ”dam break on a wet domain”, comparing the result from four different numerical schemes to the analytic solutions. Whereas the KP and CDKLM schemes are able to capture the shock solution, FBL becomes unstable, and the CTCS scheme gives different results for different choices for A. Here we have used $A = 0.1$, but no values of A give the analytic results.

Table 2: Parameters used in the oceanographic test cases. Here, (N_x,N_y) denote the number of cells or grid points within the grid, and $(\Delta x,\Delta y)$ denotes the size of each cell or distance between grid points. The interesting features of each of the cases are centered in (x_0,y_0). The surface elevation, and volume transport in x- and y-direction are given by η, hu, and hv, respectively, with initial conditions given at time t_0. The solution is developed forward in time with time-step Δt until time T. The other parameters describe ocean depth (H), gravitational force (g), Coriolis forcing (f), and eddy viscosity parameter A for CTCS. Where applicable, f_0 and β are parameters in the Coriolis beta-plane model, and α describes the slope of the ocean bed. We have used the same time-step size for all schemes.

	Test cases			
	B and C: Rossby adjustment	**D: Kelvin waves**	**E: Planetary Rossby waves**	**F: Topographic Rossby waves**
(N_x,N_y)	$(800,1000)$	$(1000,200)$	$(400,400)$	$(400,400)$
$(\Delta x,\Delta y)$	$(50\,\text{km},50\,\text{km})$	$(5\,\text{km},10\,\text{km})$	$(20\,\text{km},20\,\text{km})$	$(20\,\text{km},20\,\text{km})$
(x_0,y_0)	$(20\,000\,\text{km},25000\,\text{km})$	$(2502.5\,\text{km},-5\,\text{km})$	$(6400\,\text{km},4000\,\text{km})$	$(6400\,\text{km},4000\,\text{km})$
Δt	$100\,\text{s}$	$25\,\text{s}$	$100\,\text{s}$	$100\,\text{s}$
$\eta(x,y,t_0)$	Eq. (4.1)	Eq. (4.3) with $\eta_0=\{0.05\,\text{m},2.0\,\text{m}\}$	Eq. (4.7)	Eq. (4.7)
$hu(x,y,t_0)$	0	Eq. (4.5)	Eq. (4.8)	Eq. (4.8)
$hv(x,y,t_0)$	0	0	Eq. (4.9)	Eq. (4.9)
$H(x,y)$	$1000\,\text{m}$	$100\,\text{m}$	$25\,\text{m}$	Eq. (4.10)
g	$9.81\,\text{m/s}^2$	$9.81\,\text{m/s}^2$	$9.81\,\text{m/s}^2$	$9.81\,\text{m/s}^2$
f	$1.2\cdot10^{-4}\,\text{s}^{-1}$	$1.2\cdot10^{-4}\,\text{s}^{-1}$	Eq. (4.6)	$8.0\cdot10^{-4}\,\text{s}^{-1}$
f_0	-	-	$8.0\cdot10^{-4}\,\text{s}^{-1}$	-
β	-	-	$2.0\cdot10^{-11}\,(\text{ms})^{-1}$	-
α	-	-	-	$2.5\cdot10^{-7}\,\text{m}^{-1}$
A	0	25	0	0
T	$1.257\cdot10^7\,\text{s}$	$10\frac{\Delta x N_x}{\sqrt{gH}}\approx1.6\cdot10^6\,\text{s}$	$6.0\cdot10^6\,\text{s}$	$6.0\cdot10^6\,\text{s}$
Boundary conditions	Flow relaxation scheme, Eq. (3.14) and (3.15)	North/South: Wall, Eq. (3.12) East/West: Periodic, Eq. (3.13)	Flow relaxation scheme, Eq. (3.14) and (3.15)	Flow relaxation scheme, Eq. (3.14) and (3.15)

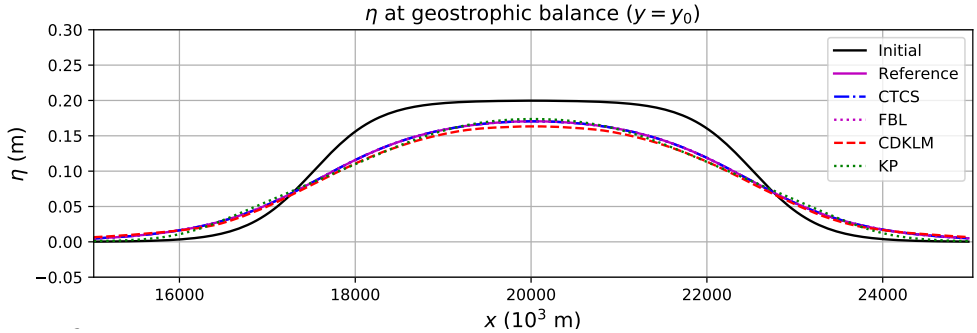

Figure 7: Case B: Steady-state results for Rossby adjustment on a flat bathymetry. The initial condition for η is shown in black. All simulators give results close to the reference solution, with slightly better results for FBL and CTCS than for KP and CDKLM.

The boundary conditions are set to allow gravity waves to leave the domain according to (3.14) and (3.15), and the solution should converge to a steady state consisting of a wide rotating bump (satisfying the Klein-Gordon equation (A.37) in A).

The domain consists of 800×1000 cells with $\Delta x = \Delta y = 50\,\text{km}$. The depth is chosen to be $H = 1000\text{m}$, and the full set of parameters are listed in Table 2, along with $D = 50\Delta x$, $L = 15\Delta x$ and $\eta_0 = 0.2$ m for (4.1). The steady-state solutions along $y = y_0$ at time T are shown in Figure 7. The reference solution is obtained by solving the Klein-Gordon equation (A.37) by a finite-difference approach, with the given initial condition and $\eta = 0$ along the boundaries. All four schemes qualitatively capture the same steady-state solution defined through the geostrophic balance.

The relative discrepancy between the simulated results and the solution of the Klein-Gordon equation, is shown in Figure 8. The finite-volume schemes are off by up to 4%, and the staggered finite-difference schemes are within machine precision of the reference.

Figure 9 explores the radial symmetry of the steady-state solutions. The dense collection of bright yellow dots represent values of η at grid points in a straight eastward line from (x_0, y_0), whereas darker blue dots represent all other grid point values. The x-axis represents the Euclidean distance from (x_0, y_0). Perfect radial symmetry would result in all the blue dots disappearing behind the yellow dots. Small deviations are present for all schemes, with CTCS and FBL being slightly better than CDKLM and KP. It should also be noted that we have observed small numerical oscillations in the steady-state solution produced by CDKLM, which we have not been able to reproduce for the other non-steady-state test cases.

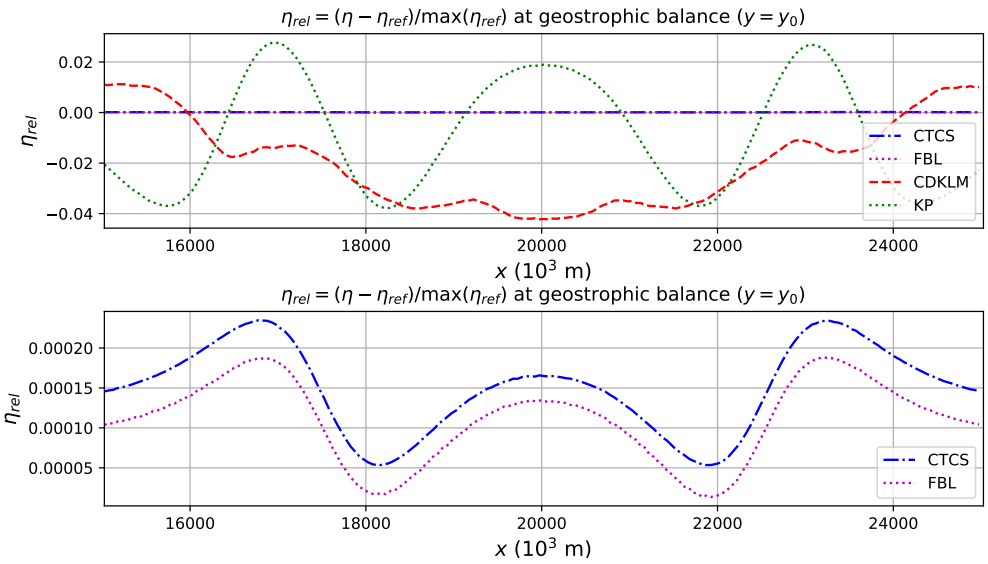

Figure 8: Case B: Discrepancy between the obtained steady-state solutions and the reference solution for the Rossby adjustment problem. The KP and CDKLM schemes obtain a steady state with a relative error of 4% compared with the reference solution. The CTCS and FBL schemes capture the reference solution with machine precision.

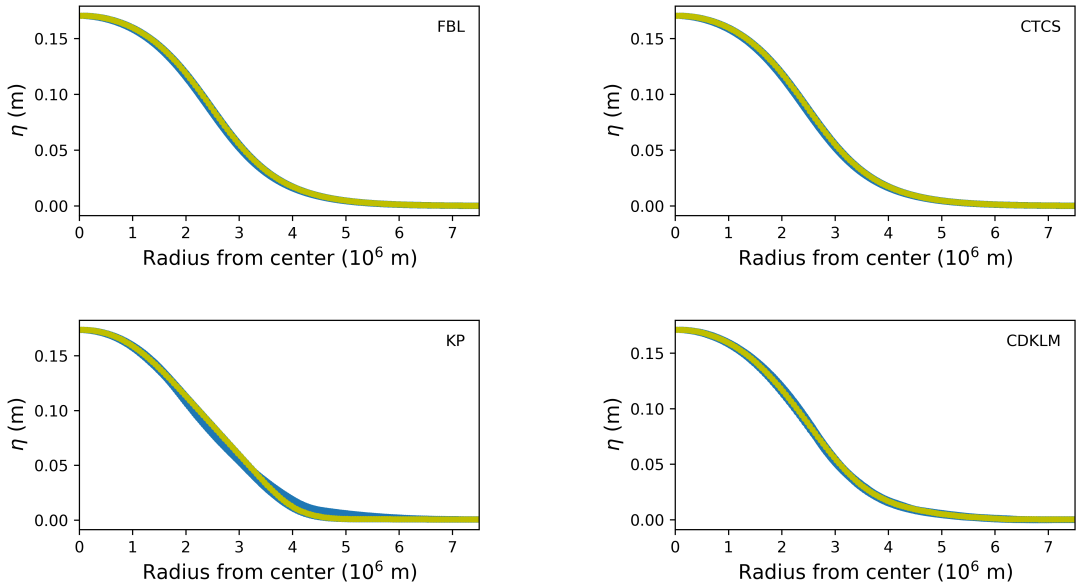

Figure 9: Case B: Radial symmetry at geostrophic balance, obtained from the Rossby adjustment problem on flat bathymetry. The bright yellow line is the η-values obtained along a straight line eastwards from the center of the domain, while the darker blue area consists of a scatter plot of all η-values radially distributed from the same center point. Deviations of the blue scatter from the yellow line indicate radial asymmetry. It is therefore clear that FBL and CTCS are slightly better than KP and CDKLM at preserving radial symmetry.

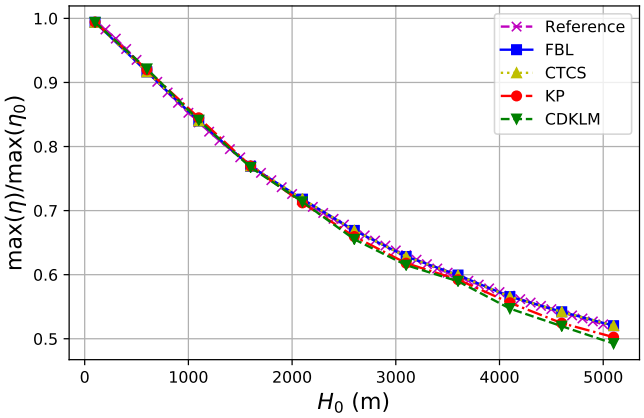

Figure 10: Case C: Relative height of the Rossby adjustment steady state η obtained by the different schemes for different depths, compared with a reference solution. The FBL and CTCS schemes give good match, whereas the KP and CDKLM schemes have slightly too low steady state bumps for large depths.

4.3 Case C: The Adjustment Problem for Variable Rossby Radius of Deformation

This case checks the schemes ability to capture how the Rossby radius of deformation in Case B depends on water depth. We vary H_0 from 100 to 5000 m, and study the ratio between the maximum steady state surface elevation and the maximum initial surface elevation. Initial and boundary conditions are the same as for Case B.

The phase speed c of free gravity waves increases with depth, and hence the Rossby radius $L_R = c/f$ also increases. The relevant parameter here is the ratio between the horizontal scale of the initial surface elevation and the Rossby radius. With increasing depth, the Rossby radius increases compared with the fixed initial disturbance. This means that more potential energy is converted to kinetic energy in the form of gravitational waves that propagate away. The geostrophically balanced steady-state solution therefore becomes distributed over a larger area. We would expect that the maximum surface elevation in the steady-state solution decreases as the depth and the Rossby radius increases. Such reduction is exactly what is seen when calculating the reference solution for different water depths using the same method as in Case B.

Figure 10 shows the experimental results for all four numerical schemes. The FBL and CTCS schemes result in almost identical steady-state solutions for all values of H_0, with a very good match to the reference solution. The finite-volume methods on the other hand, give slightly lower steady-state solutions for the surface elevation for the deep cases. This difference indicates that the finite-volume methods may be more diffusive. We will discuss this possibility in relation to Cases E and F.

4.4 Case D: Kelvin Waves

Kelvin waves are shallow-water waves trapped along the coast that propagate with the cost on their right / left side on the the northern / southern hemisphere. For this case, we consider a rectangular domain with constant depth, wall boundary conditions, (3.12), along the southern and northern boundaries, and a periodic boundary condition, (3.13), over the east-west boundary. The initial state consists of a wave trapped at the southern boundary and travelling eastwards. The initial surface elevation is

$$\eta(x,y,t_0) = \frac{\eta_0}{2}\exp\left(\frac{-\sqrt{(y-y_0)^2}}{L_R}\right)\left[1.0+\tanh\left(\frac{-\sqrt{(x-x_0)^2}+L_R}{L_R/3}\right)\right], \tag{4.3}$$

and the momentum is based on the geostrophic balance, (A.3), expressed with respect to the conserved variables as

$$hu(x,y) = -\frac{gH}{f}\frac{\partial \eta}{\partial y} \quad \text{and} \quad hv(x,y) = \frac{gH}{f}\frac{\partial \eta}{\partial x}. \tag{4.4}$$

In the case of Kelvin waves, the momentum is balanced according to (4.4) along the barrier, where hv is set to zero. Using (4.3), we get that

$$hu(x,y,t_0) = \sqrt{gH}\cdot\text{sign}(y-y_0)\eta(x,y,t_0), \tag{4.5}$$

$hv(x,y,t_0) = 0$. We let $(x_0,y_0) = (2502.5\text{km}, -5\text{km})$, which is chosen so that the maximum height of the wave is in a cell center in the middle of the domain in x-direction, and the wave height is still increasing in the y-direction as it meets the southern boundary. The amplitude of the wave is given by η_0, and we will use two different values for η_0 in this test case. All other parameters are listed in Table 2.

From linear wave theory, as discussed in A, Kelvin waves are standing waves travelling with speed $\sqrt{gH}$ along the coast. By selecting a small amplitude, $\eta_0 = 0.05\,\text{m}$, we expect approximately linear behavior even from the nonlinear equations, and the period in our domain becomes $T = \Delta x N_x/\sqrt{gH}$. Figure 11 shows the resulting Kelvin waves for all four schemes as cross sections along the x-axis, focusing on the middle section of the domain after one, five and ten periods. The solid lines represent $\eta(x,\frac{1}{2}\Delta y,t)$ along the southern boundary and the dotted lines show $\eta(x,(30+\frac{1}{2})\Delta y,t)$ some distance away from the boundary. The waves have momentum towards the right. We see that FBL, CTCS and CDKLM give close linear advection as expected. If we look carefully, however, we note that there are tendencies of oscillation at $t = 10T$, with a wave building up on the front of the wave, and a depression just behind the wave. This is a typical artifact of such schemes [30], and is exaggerated for coarser resolutions. The KP scheme also maintains the periodicity in the solution, but the amplitude of the Kelvin wave is decreasing, and an edge builds up behind the wave. This is most likely caused by the naïve discretization of the Coriolis forcing term.

Next, we look at Kelvin waves with a larger amplitude by setting $\eta_0 = 2.0$m, and these results are shown in Figure 12. As expected, the FBL scheme produces the same periodic solution as for the small amplitude wave, as it solves the linearized equations. The other three schemes solve the nonlinear equations where the wave speed is a function of the full depth $H+\eta$ (meaning that the particle velocity is expected to larger on the crest of the wave), and we expect that the wave should sharpen towards a shock with time. This is the behavior observed by the KP and CDKLM schemes, shown in the two lower panels of Figure 12, and the same tendency can also be observed for CDKLM in Figure 11. CTCS, on the other side, is not able to produce this solution, and instead produces a solution with the opposite behavior, as seen in the second panel of Figure 12. Here, the crest of the wave is travelling slower due to numerical dispersion, which is a known property of the CTCS scheme [19, 40]. The consequence is that the phase speed slows down, and generates a shock behind the wave. We have been able to reproduce this behaviour for a wide range of values for the eddy viscosity parameter, A, and since CTCS is unable to maintain shock solutions, the shock results in spurious oscillations.

In total, we see that the FBL, KP and CDKLM schemes behave as expected from a physical point of view, and CTCS behaves as expected from a numerical point of view. The finite-volume methods are better at maintaining fast-travelling waves than the CTCS scheme. It should also be noted that the behavior from the results in Figure 12 can be reproduced for pure gravity waves in non-rotating domains as well.

4.5 Case E: Planetary Rossby Waves

The two last test cases focus on dynamics related to potential vorticity, which is defined as the total vertical vorticity divided by the total water depth. The total vorticity can be split into two parts: one dominating planetary part caused by Earth's rotation and a relative part caused by the local vorticity of the flow in the rotating reference frame. The potential vorticity expresses the angular momentum of a material water column, and its conservation causes the spin of a water column to increase if the column is stretched vertically and vice versa. Large-scale changes in the relative vorticity are due to horizontal wind shear and are important for the basin-scale circulation in the oceans. Changes in the relative vorticity can also occur on smaller scales when a column of water is advected into deeper or shallower areas. Changes in the planetary vorticity occurs when a water column is advected either northwards or southwards because the vertical component of the Earth's rotation (the Coriolis parameter f) is different. In non-dissipative systems, and in the absence of atmospheric forcing, the potential vorticity is conserved.

Disturbances in the vorticity may induce a class of waves referred to as Rossby waves. If changes in the vorticity are associated with varying bathymetry, we obtain so-called topographic Rossby waves that propagate along lines of constant depth. Alternatively, we can obtain planetary Rossby waves for which gradients in the local rotation rate f determine the propagation characteristics. These waves have a primary component in the zonal direction, and a brief description of the relevant (linearized) theory is provided

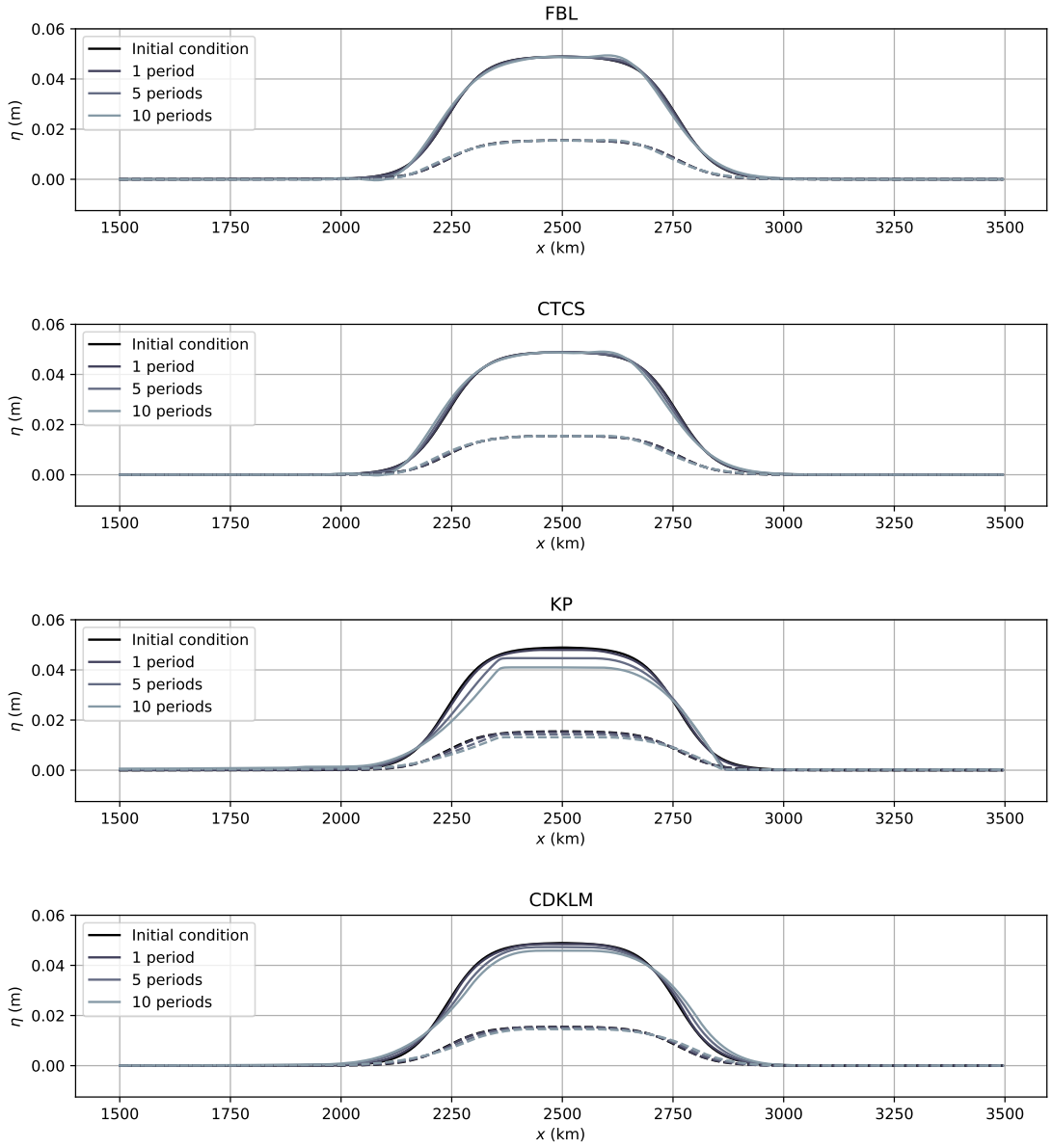

Figure 11: Case D with small waves: Small amplitude Kelvin waves travelling along the southern wall boundary, in a east-west periodic domain. The solid lines represent values of η along the boundary, while the dotted lines show η 30 grid cells into the domain. The initial state and the solution after one, five and ten periods are plotted. The small amplitude of the wave gives approximately linear behavior for all four schemes, but we see that the wave produced by the KP scheme is decreasing with an unnatural edge at the back of the wave.

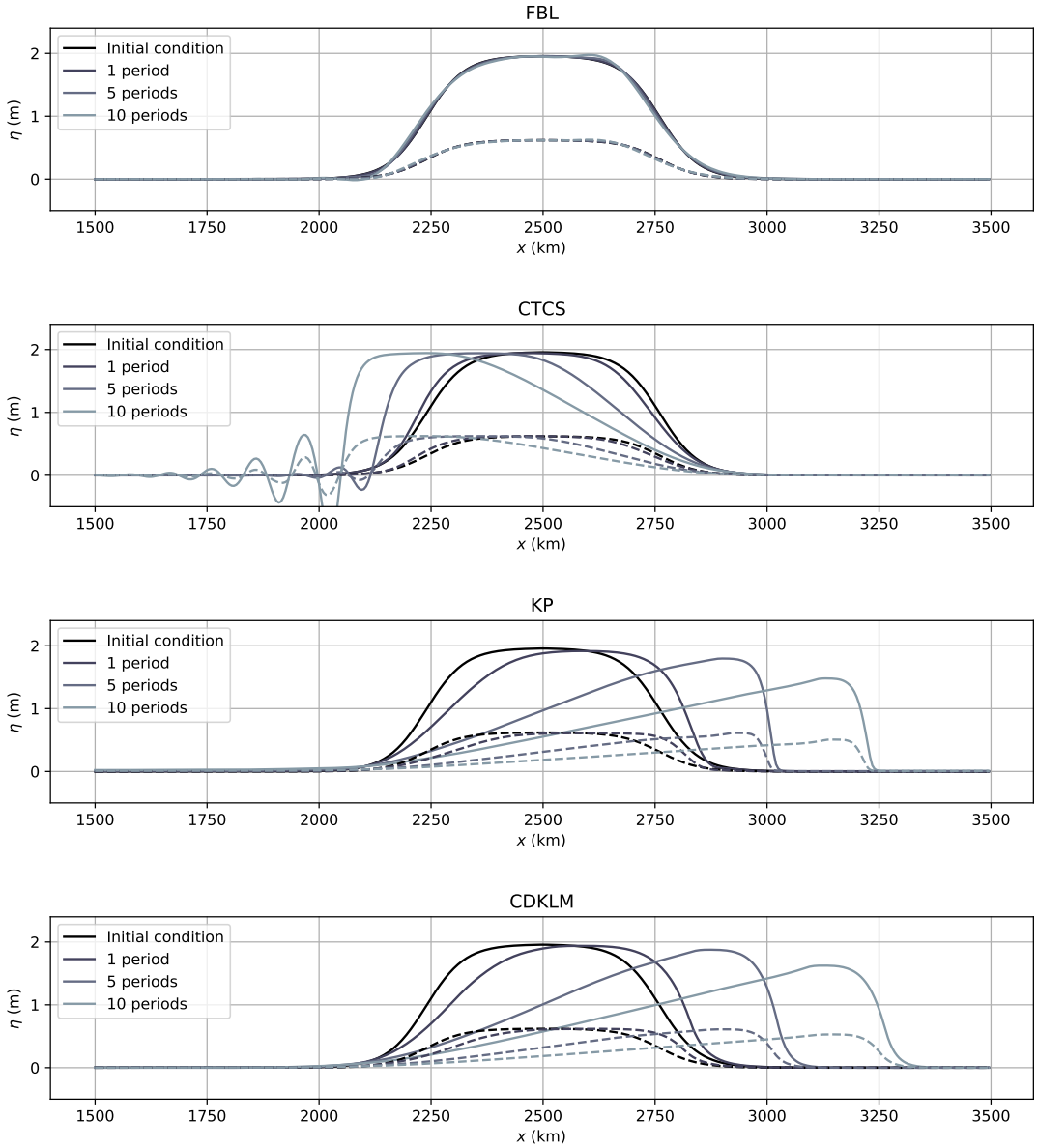

Figure 12: Case D with large waves: Kelvin waves travelling along the southern wall boundary, in a east-west periodic domain. The solid lines represent values of η along the boundary, while the dotted lines show η 30 grid cells into the domain. The initial state and the solution after one, five and ten periods are plotted. The figure shows that FBL gives results according to linear wave theory. In the nonlinear equations, the top of the wave is expected to have a higher phase speed than the slopes of the wave, causing a shock to be slowly generated. This behavior is well captured by the KP and CDKLM schemes, but the CTCS scheme is slowed down due to numerical dispersion.

in A.

Planetary Rossby waves depend on variations in the local rotation rate f. In these test cases, we consider a beta-plane model of the Coriolis force, given by

$$f(y) = f_0 + \beta(y - y_0). \tag{4.6}$$

Here, f_0 is the Coriolis force at y_0, defined as $f_0 = 2\omega\sin(\phi_0)$, in which $\omega = 2\pi/(24\text{hours})$ is the angular velocity of the Earth and ϕ_0 is the latitude at y_0. The parameter β is hence

$$\beta = \frac{\partial f}{\partial y} = \frac{2\omega}{R}\cos(\phi_0),$$

in which R is the radius of the Earth.

In the following test case, y_0 is chosen at approximately 33° north in the center of the domain, giving the values for f_0 and β presented in Table 2. The domain is chosen to consist of 400×400 cells with $\Delta x = \Delta y = 20\,\text{km}$, with a depth of $H = 25\,\text{m}$. The initial disturbance is a Gaussian bump,

$$\eta(x,y,t_0) = \eta_0 \exp\left\{ -\frac{(x-x_0)^2 + (y-y_0)^2}{r_0} \right\}, \tag{4.7}$$

with $\eta_0 = 0.25\,\text{m}$, $(x_0, y_0) = (0.8\Delta x N_x, 0.5\Delta y N_y)$, and $r_0 = 2.5 \cdot 10^6\,\text{m}^2$. To avoid that most of the potential energy from the bump results in gravity waves, the initial momentum is constructed by inserting (4.7) into the geostrophic balance (4.4). The initial momentum then becomes

$$hu(x,y,t_0) = 2\frac{gH(y-y_0)}{f_0 r_0}\eta(x,y,t_0), \tag{4.8}$$

and

$$hv(x,y,t_0) = -2\frac{gH(x-x_0)}{f_0 r_0}\eta(x,y,t_0). \tag{4.9}$$

Flow relaxation boundary conditions are used, and all parameters are summarized in Table 2.

Simulation results of planetary Rossby waves from all four schemes are shown in Figure 13. The right-hand panels show the final state of η at time $t = 6.0 \cdot 10^6$ s, corresponding to approximately 70 days (60 000 time-steps). From the initial disturbance, we can see the Rossby waves propagating westwards, with significant components in the north-south direction. All schemes tend to generate Rossby waves with larger amplitudes to the north than to the south, where the Coriolis force is weaker. The left-hand side panels in Figure 13 are Hovmöller diagrams, which illustrate how the waves develop and propagate along the x-axis at $y = y_0$ over time. From these diagrams we may note that the Rossby waves propagate from east to west as theory predicts. This can be seen from the lines of constant phase that extend upwards to the left. We also see that there are two dominating modes with different phase speeds, and that the wave energy

slowly propagates eastwards; that is, the x-components of the group and phase velocities have different signs.

Because the test case is two-dimensional, there are no simple analytical solutions to use as reference. We would, however, expect the CTCS scheme to perform quite well, since this scheme is specifically tailored for problems such as the one considered here. We note in particular that the KP scheme has a much higher dissipation rate than the other schemes. This may be caused by the naïve discretization of the Coriolis source terms in the KP scheme.

4.6 Case F: Topographic Rossby Waves

The wave phenomena shown in Case E can also be produced by varying the bottom topography rather than the Coriolis force, and is then called topographic Rossby waves. We have here chosen parameter values so that the topographic Rossby waves should (roughly) correspond to the planetary Rossby waves considered above. The bathymetry is modelled as a linear function of the form

$$H(x,y) = H_0[1-\alpha(y-y_0)]. \tag{4.10}$$

Here, y_0 and H_0 are chosen to be the same as for the case with planetary Rossby waves, and we use constant $f(y) = f_0$. The slope parameter for the bottom, α, is chosen according to the Coriolis force in the above case, so that $\alpha = \beta/f_0$ (see A for details). The domain, and boundary and initial conditions are chosen to be the same as in the planetary case.

Simulation results for the topographic Rossby waves are shown in Figure 14, with Hovmöller diagrams on the left-hand side and η after the last time-step on the right-hand side. Again, there is no simple analytical solution to use as reference, and we cannot expect the topographic and planetary Rossby wave cases to be identical. The solutions are qualitatively similar, with westward propagating waves (two main modes) and eastward propagating wave energy, but the solutions are more symmetric across the centerline $y = y_0$.

The three schemes FBL, CTCS, and CDKLM give results that are quite similar to each other, while the KP scheme is dissipative in the same way as for the planetary Rossby waves. The overall amplitudes are somewhat smaller for CDKLM than for the two staggered schemes.

4.7 Numerical Order and Performance

We have determined the numerical order of convergence for the four different numerical schemes. The test case is a smooth problem that avoids the formation of shocks during the simulation period and consists of an initial radial cosine bump at the center of the domain with zero momentum and wall boundary conditions. The domain measures 512×512 km, with a gravitational coefficient of 9.81 m/s^2, a Coriolis coefficient of 0, and

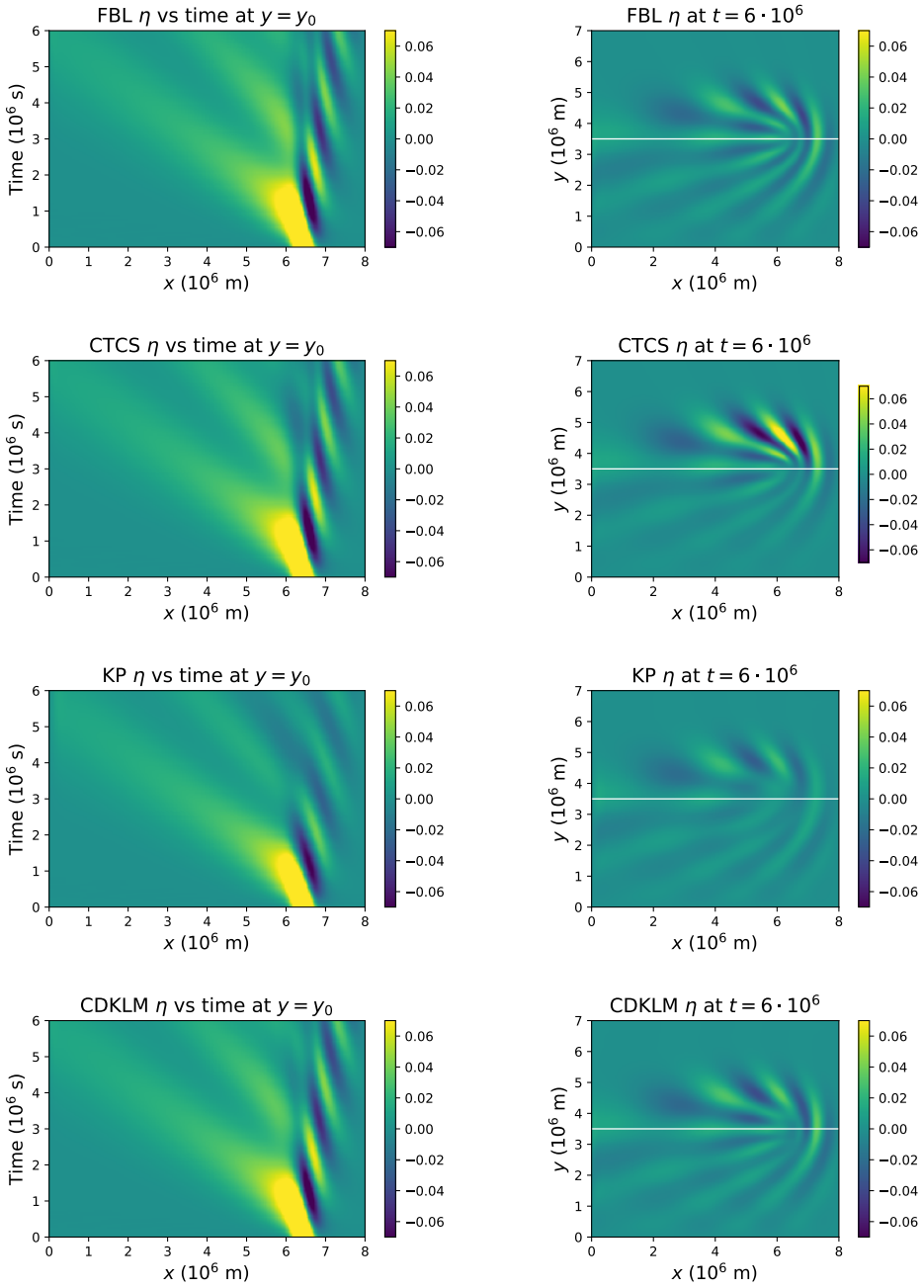

Figure 13: Case E: Long-term simulation results when investigating planetary Rossby waves caused by a linear Coriolis parameter. The left-hand figures show Hovmöller diagrams located along y_0. The figures at the right-hand side show η after the last time-step, with the cross section at y_0 illustrated with a white line. Note that KP has a more dissipative solution than the others, as the eastwards energy is lost in this scheme. Note also that the solutions are not symmetric about y_0.

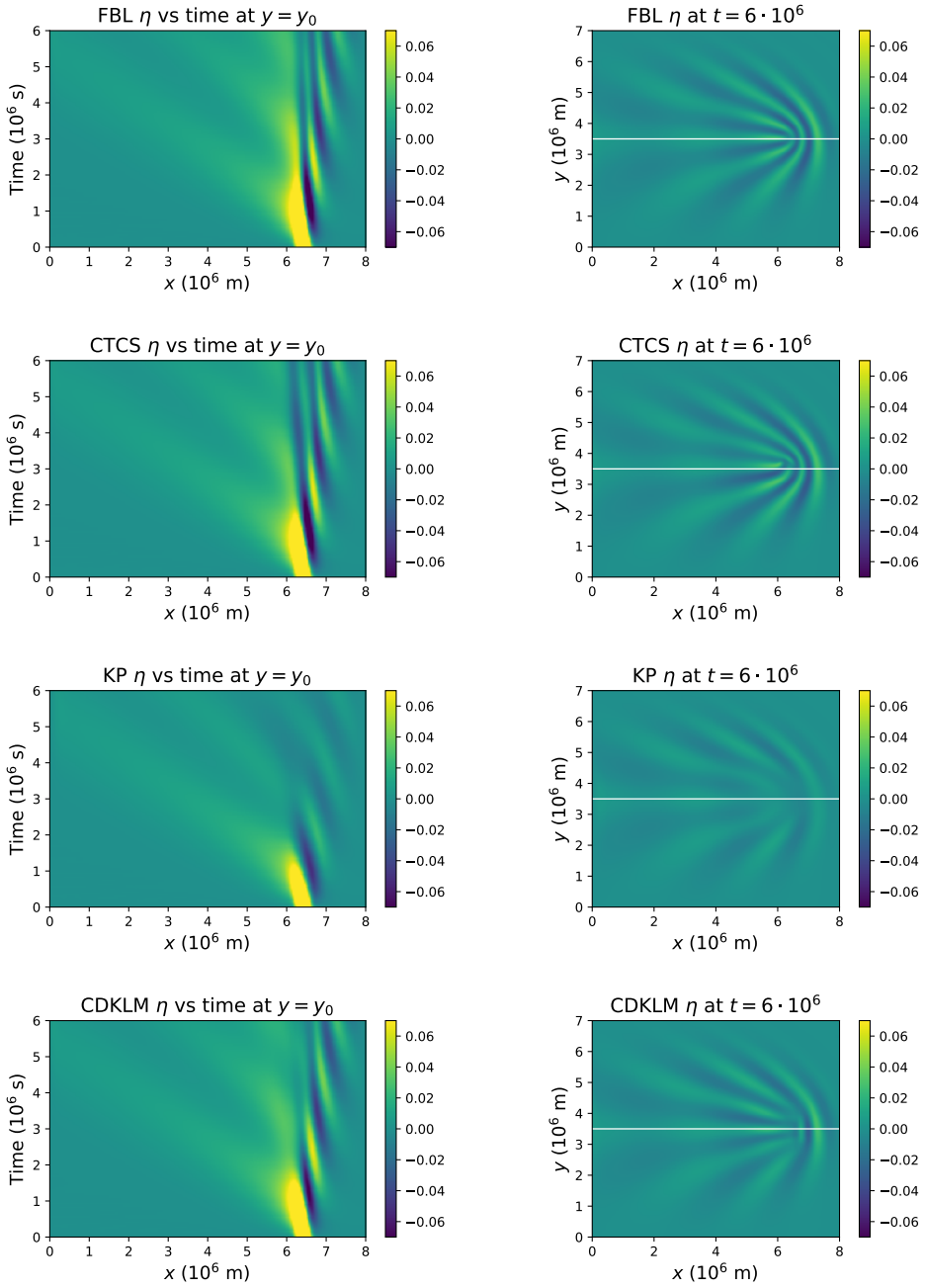

Figure 14: Case F: Long-term simulation results for topographic Rossby waves caused by the bathymetry given in (4.10). Hovmöller diagrams for y_0 are shown to the left, and η at the last time-step to the right. The white lines on the right-most figures illustrate the cross section at y_0. The solutions for FBL, CTCS, and CDKLM are very similar, whereas KP is more dissipative. The results here are more symmetric around y_0 than the planetary Rossby waves in Case E.

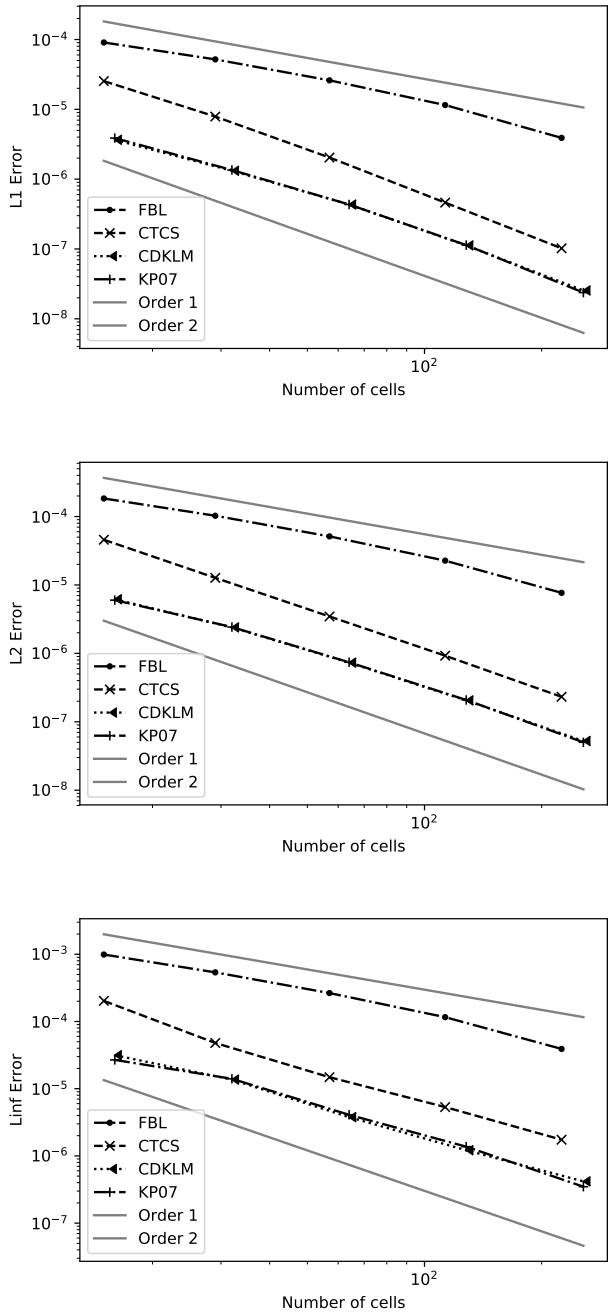

Figure 15: Numerical order of convergence for the four different schemes for η, displaying the expected L^1, L^2, and L^∞ error convergence rates (first order for FBL, and second order for the rest). The median of the L^1 convergence rate over the interval is 1.11, 2.09, 1.79, and 1.78 for FBL, CTCS, KP and CDKLM, respectively. The numerical L^2 convergence is 1.11, 1.94, 1.77, and 1.77, and for L^∞ the numerical convergence rate is 1.13, 1.70, 1.68, and 1.61.

constant depth $H_0 = 50$ m. The radial cosine bump is defined as

$$\eta_{j,k} = \begin{cases} \frac{1}{2}\eta_{\max}\left(1+\cos\left(\frac{r}{c}\pi\right)\right), & \forall r \leq c \\ 0, & \forall r > c, \end{cases}$$

in which $\eta_{\max} = 1.0$ cm, r is the distance from the center of the domain, and c is the radial size of the bump, in our case 60% of the domain width. For the finite-volume schemes, we start by generating a fine scale initial η, and integrate the variables over the coarse grid cells to make sure we solve the exact same initial conditions. For the finite-difference schemes we simply evaluate the point values on the cosine bump. We then simulate until $t = 30$ minutes, and compute the difference between the fine scale reference and the coarse scale simulation. The reference is generated by simulating on a fine mesh, and the fine-scale solution is then coarsened using the same method as for the initial conditions. The error norms have been computed in double precision.

The results are shown in Figure 15, showing second-order convergence for all schemes except FBL, as expected. It should be noted that CTCS is a leapfrog scheme that is only second order accurate every other time-step (see e.g., [40]).

Practical oceanographic simulation is demanding on computational capacity, and it is therefore important that the numerical schemes allow for fast and efficient implementations, especially for ensemble-based simulation. It has previously been shown that explicit finite-difference and finite-volume schemes, such as those considered herein, have an inherent parallelism that can readily be exploited in many-core computing [4, 5, 10, 24, 26]. The actual performance of each scheme will in general vary upon the specific simulation case, domain size, hardware, and level of optimization, and we therefore choose to normalize all performance values with respect to the fastest non-linear scheme (CTCS). To evaluate the computational performance we run the above case on a grid consisting of 2048×2048 cells for $t = 24$ hours, using a time-step that incorporates each scheme's CFL condition respectively, with a Courant number of 0.9. All the schemes have been been optimized to a comparable level, and are run with optimal configurations [3]. By comparing the wall clock time for each scheme, we see that CTCS completes the simulation roughly $4.3\times$ and $5.7\times$ faster than KP and CDKLM, respectively. By looking at iterations per second, we see that KP and CDKLM requires $3\times$ and $4\times$ as much time for each time-step, respectively, compared to CTCS. Note that the difference between these two measures corresponds to the difference in CFL conditions between CTCS and the two finite-volume schemes. The linearized equations solved by FBL runs 60% faster than CTCS, and this is mainly due to the differences in their CFL conditions. In terms of memory requirement, all three non-linear schemes store the state vector $[\eta, hu, hv]$ for two successive time-steps, whereas FBL only requires the state for one time-step. The finite-volume schemes are also implemented by storing the equilibrium depth H at both the cell centers and cell intersections, whereas the finite-volume schemes store H in the cell centers only. All these performance measures are summarized in Table 3.

4.8 Comparison

Table 3 summarizes the four schemes for the presented test cases. The table is divided into three groups, where the first group is related to general characteristics valid for rotational and non-rotational settings alike. The second group covers the oceanographic aspects, and the third reports on the numerical implementation.

All schemes conserve mass and momentum within the domain, and preserve lake-at-rest solutions. The finite-difference schemes, however, break down for solutions containing shocks. Even though shock solutions do not naturally occur in the ocean, the dam break test has been included here as it is highly useful to be aware of such limitations for the schemes at hand.

In the second group, we see that FBL and CTCS are able to capture the Rossby adjustment steady-state solution better than KP and CDKLM. All schemes except for KP are able to represent Kelvin waves of small amplitudes according to linear wave theory. Larger differences are seen as the amplitude is increased so that nonlinearities dominate the simulations. The finite-volume schemes capture the physical expected solution, with a shock forming in front of the wave. CTCS, however, gives a solution where the crest of the wave is slowed, resulting in a shock behind the wave. FBL maintains a linear solution, as is expected by the scheme. In the cases of planetary and topographic Rossby waves, FBL, CTCS and CDKLM give qualitatively the same solutions in accordance with theory, whereas KP is significantly more dissipative.

The final group considers computational aspects of the schemes. We note that the performance of CTCS is significantly better than KP and CDKLM, mainly due to more efficient scheme, and partly due to less strict CFL conditions. Finally, we note that all four schemes obtain the expected numerical order.

5 Summary and Conclusions

We have in this paper evaluated four numerical schemes for solving the rotational shallow-water equations by looking at six oceanographic test cases. The test cases have been chosen based on oceanographic concepts important for transient flow, and investigate each scheme's ability to produce and maintain geostrophic steady-state solutions (Rossby adjustment), capture fast coastal waves (Kelvin waves), and capture slow waves due to variations in the potential vorticity (Rossby waves). Two of the selected numerical schemes are the traditional finite-difference methods FBL and CTCS, evaluated on staggered grids arising from the oceanographic community. The last two schemes, KP and CDKLM, are recent finite-volume methods that have been developed within the community working on high-resolution schemes for more general hyperbolic conservation laws. These schemes have been chosen as they all have favorable properties with respect to doing ensemble-based simulations, e.g., for storm surges, and/or data assimilation for drift prediction.

Our findings show that the FBL scheme gives the expected linear results for all test

Table 3: Comparison of numerical schemes, based on quantitative and qualitative properties. The rows are grouped as follows: General characteristics, oceanographic characteristics, and computational characteristics. The performance-related values are obtained from running a case consisting of 2048×2048 cells, and are normalized with respect to CTCS.

	Numerical Scheme			
	FBL	**CTCS**	**KP**	**CDKLM**
Preserve lake-at-rest	Yes	Yes	Yes	Yes
Accurately capture shocks	No	No	Yes	Yes
Case B and C: Rossby adjustment	Good	Good	Fairly good	Fairly good
Case D: Kelvin waves	Good	Medium	Medium	Good
Case E: Planetary Rossby waves	Good	Good	Medium	Good
Case F: Topographic Rossby waves	Good	Good	Medium	Good
Numerical L^2 convergence rate	1.11	1.94	1.77	1.77
Relative simulation wall time	0.4	1.0	4.3	5.7
Relative iterations per second	1.25	1.0	0.33	0.25
Memory req. for 2048×2048 cells	64.1 MB	112.3 MB	128.5 MB	128.5 MB

cases, and is the most computational efficient scheme due to its simplicity. For the full nonlinear equations, we see that CTCS performs well in cases dominated by geostrophic balance, such as Rossby adjustment and Rossby waves, but gives incorrect dispersion for large gravity-driven waves. The naïve discretization of the Coriolis force in the KP scheme results in a too diffusive scheme, causing it to perform worse than the CDKLM scheme for all test cases. The CDKLM scheme, although more expensive than KP, gives good results on all test cases, and is shown to be superior for capturing gravity-driven motion, such as the Kelvin waves, but there are still potential for even better treatment of the geostrophic balances.

Code Availability

The software used in this research is published as supplementary material [21] under DOI 10.5281/zenodo.3204200.

Acknowledgements

This work is supported by the Research Council of Norway through grant number 250935 (GPU Ocean). The authors would also like to thank Knut-Andreas Lie and Lars Petter Røed for valuable comments and discussions.

A Oceanographic Background

The purpose of this appendix is to provide a physical outline of the planetary and topographic Rossby waves and the Rossby adjustment problem. All cases start with a disturbance in sea surface height and develop under strong dominance of the rotation. For the Rossby adjustment, one reaches a steady state, whereas the Rossby waves will create waves propagating out from the origin of the disturbance. Notably, the restoring force for rotationally dominated large waves is conservation of total potential vorticity. The following description can be found in several text books on large-scale fluid dynamics, but is provided here for the convenience of the readers.

A.1 Coriolis force

The Coriolis parameter is defined as

$$f = 2\Omega \sin(\phi), \tag{A.1}$$

in which Ω is the Earth's rotation rate and ϕ is the latitude. Hence $|f|$ is zero at the equator and attains its maximum values on the poles. Denoting the horizontal velocity components (u,v) in the west-to-east (x) and south-to-north (y) directions, respectively, the Coriolis force per unit density is

$$\begin{aligned} F_f^{(x)} &= fv, \\ F_f^{(y)} &= -fu. \end{aligned} \tag{A.2}$$

The dominating force balance in the ocean is the geostrophic balance, which equates the pressure gradient force and the Coriolis force. For barotropic flows, the pressure gradient force is due to surface tilt. If we define the surface coordinate as $z = \eta(x,y,t)$, the barotropic geostrophic balance is then expressed mathematically as

$$\begin{aligned} -fv &= -g\frac{\partial \eta}{\partial x}, \\ fu &= -g\frac{\partial \eta}{\partial y}, \end{aligned} \tag{A.3}$$

in which g is the acceleration due to gravity.

A.2 Potential Vorticity

By neglecting friction and the nonlinear term in the pressure gradient, the equations for barotropic velocities $\boldsymbol{v}_h = (u,v)$ and continuity read

$$\frac{\partial u}{\partial t} + u\frac{\partial u}{\partial x} + v\frac{\partial u}{\partial y} - fv = -g\frac{\partial \eta}{\partial x}, \tag{A.4}$$

$$\frac{\partial v}{\partial t} + u\frac{\partial v}{\partial x} + v\frac{\partial v}{\partial y} + fu = -g\frac{\partial \eta}{\partial y}, \tag{A.5}$$

$$\frac{\partial \eta}{\partial t} + \frac{\partial}{\partial x}[(H+\eta)u] + \frac{\partial}{\partial y}[(H+\eta)v] = 0. \tag{A.6}$$

Taking the curl of (A.4) and (A.5), we obtain

$$\frac{d}{dt}(\zeta + f) = -(\zeta + f)\left(\frac{\partial u}{\partial x} + \frac{\partial v}{\partial y}\right), \tag{A.7}$$

where $d/dt \equiv \partial/\partial t + u(\partial/\partial x) + v(\partial/\partial y)$ is the total derivative and $\zeta = \partial v/\partial x - \partial u/\partial y$ is the vertical component of the vorticity. (A.7) describes conservation of angular momentum. If depth does not change in time, we can rewrite (A.6) as

$$\frac{d}{dt}(H+\eta) = -(H+\eta)\left(\frac{\partial u}{\partial x} + \frac{\partial v}{\partial y}\right). \tag{A.8}$$

Note the similarities between (A.7) and (A.8): both the vorticity and the total height of a material water column depend on the convergence/divergence of the flow field. Combining these equations, we find that

$$\frac{d}{dt}\left(\frac{\zeta + f}{H+\eta}\right) = 0. \tag{A.9}$$

The potential vorticity $(\zeta + f)/(H+\eta)$ is a conserved quantity in non-dissipative flows in a rotating reference frame. To clarify any discussion when using potential vorticity, ζ is generally referred to as the relative vorticity, and f as the planetary vorticity. (A.9) implies that the flow will tend to follow contours of constant f/H, since these are the dominating terms in geophysically relevant cases.

A.3 Kelvin waves

Waves influenced by earth rotation and leaning on a topography are known as Kelvin waves, and are very important for explaining a number of phenomena such as tides and coastal transports. Here we will accordingly consider a simple derivation of the main characteristics of these waves. Observations reveal that the velocity parallel to the coast is much larger than the velocities perpendicular to the coast. Assuming a coast along the

x-axis and that $V \ll U$ (and assuming U, V have similar time scales) and that nonlinear terms are small we find the following governing equations from (A.4) and (A.5)

$$\frac{\partial U}{\partial t} = -gH\frac{\partial \eta}{\partial x}, \tag{A.10}$$

$$fU = -gH\frac{\partial \eta}{\partial y}, \tag{A.11}$$

$$\frac{\partial \eta}{\partial t} + \frac{\partial U}{\partial x} = 0. \tag{A.12}$$

Combining (A.10) and (A.12) gives

$$\frac{\partial^2 \eta}{\partial t^2} - gH\frac{\partial^2 \eta}{\partial x^2} = 0, \tag{A.13}$$

which shows that this system behaves as a wave solution moving with speed $c_0 = \pm\sqrt{gH}$ in the x-direction (later analysis will show that waves can only travel in positive x-direction). Combining (A.11) and (A.12) shows that the wave structure is governed by

$$\frac{\partial \eta}{\partial t} - \frac{gH}{f}\frac{\partial^2 \eta}{\partial x \partial y} = 0. \tag{A.14}$$

Here it may be noted that the parameter group in (A.13) can be written as the wave speed times the Rossby radius L_R,

$$L_R = \frac{\sqrt{gH}}{f} = \frac{c_0}{f}, \tag{A.15}$$

such that

$$\frac{\partial \eta}{\partial t} - L_R c_0 \frac{\partial^2 \eta}{\partial x \partial y} = 0. \tag{A.16}$$

The fact that the solution behaves as a wave in the x-direction, implies that the solution can be written as

$$\eta = G(y)F(x,t). \tag{A.17}$$

Thus, (A.16) gives

$$G\frac{\partial F}{\partial t} - L_R c_0 \frac{\partial G}{\partial y}\frac{\partial F}{\partial x} = 0, \tag{A.18}$$

or

$$\frac{\partial F/\partial t}{c_0 \partial F/\partial x} = L_R \frac{\partial G/\partial y}{G}. \tag{A.19}$$

The solutions are of the form

$$\eta \propto e^{y/L_R}F(x + c_0 t) + e^{-y/L_R}F(x - c_0 t). \tag{A.20}$$

Assuming that our solution must be limited as $y \to \infty$ implies that the solution with positive exponent must be zero. Thus, for problems unbounded in the y-direction

$$\begin{aligned} \eta &= e^{-y/L_R} F(x - c_0 t), \\ u &= \frac{g}{f L_R} F(x - c_0 t). \end{aligned} \tag{A.21}$$

These waves – referred to as Kelvin waves – travel in positive x-direction requires a coast on the right of their travel directions (for the northern hemisphere). Due to the rotation they are trapped within the Rossby radius from the coast.

A.4 Rossby Waves

Rotating systems support potential vorticity waves, or so-called Rossby waves. The dynamics of Rossby waves can more easily be studied when we assume $\eta = 0$, that is, using a rigid lid approximation. We may then introduce a stream function ψ such that

$$Hu = -\frac{\partial \psi}{\partial y}, \tag{A.22}$$

$$Hv = \frac{\partial \psi}{\partial x}, \tag{A.23}$$

which by definition fulfills the continuity equation

$$\frac{\partial}{\partial x}(Hu) + \frac{\partial}{\partial y}(Hv) = 0. \tag{A.24}$$

The conservation equation for potential vorticity, (A.9) with the rigid lid approximation, becomes

$$\frac{1}{H}\frac{\partial \zeta}{\partial t} + u\frac{\partial}{\partial x}\left(\frac{f}{H}\right) + v\frac{\partial}{\partial y}\left(\frac{f}{H}\right) = 0, \tag{A.25}$$

under the assumption $f \gg \zeta$. Using the definitions of the vorticity and stream function, the conservation of vorticity reads (see also [15], Eq. 10.12.4, p. 409)

$$\frac{\partial}{\partial t}\left[\frac{\partial}{\partial x}\left(\frac{1}{H}\frac{\partial \psi}{\partial x}\right) + \frac{\partial}{\partial y}\left(\frac{1}{H}\frac{\partial \psi}{\partial y}\right)\right] + \frac{f}{H^2}\left[\frac{\partial H}{\partial x}\frac{\partial \psi}{\partial y} - \frac{\partial H}{\partial y}\frac{\partial \psi}{\partial x}\right] + \frac{1}{H^2}\left[\frac{\partial f}{\partial x}\frac{\partial \psi}{\partial y} + \frac{\partial f}{\partial y}\frac{\partial \psi}{\partial x}\right] = 0. \tag{A.26}$$

Let us consider the case with $H = H(y)$ and $f = f_0 + \beta y$, where the latter is the so-called beta-plane approximation. Then $\partial f / \partial y = \beta$, and (A.26) becomes

$$\frac{\partial}{\partial t}\left[\frac{1}{H}\left(\frac{\partial^2 \psi}{\partial x^2} + \frac{\partial^2 \psi}{\partial y^2}\right) - \frac{1}{H^2}\frac{\partial H}{\partial y}\frac{\partial \psi}{\partial y}\right] - \frac{f}{H}\left[\frac{1}{H}\frac{\partial H}{\partial y} + \frac{\beta}{f}\right]\frac{\partial \psi}{\partial x} = 0. \tag{A.27}$$

To investigate Rossby wave dispersion further, we assume that the depth is given by the function $H = H_0 \exp(-\alpha y)$. We also assume a wave solution $\psi = A\exp[i(kx+\kappa y-\omega t)]$, where A is a constant and $\kappa = l+i\gamma$ is a complex wave number in the y-direction. From (A.27) we obtain the dispersion relation

$$\kappa^2 - i\alpha\kappa + \left(\frac{k}{\omega}(\alpha f+\beta)+k^2\right) = 0. \tag{A.28}$$

From the complex part we obtain $\gamma = \alpha/2$. The real part yields the dispersion relation

$$\omega = -\frac{k(\alpha f+\beta)}{k^2+l^2+(\alpha/2)^2}. \tag{A.29}$$

With $\alpha \neq 0$ and $\beta = 0$, we have *topographic* Rossby waves, whereas with $\alpha = 0$ and $\beta \neq 0$, we have *planetary* Rossby waves.

From (A.28), we see there is a close similarity between these types of Rossby waves when $\alpha f = \beta$, in particular for small $\alpha^2 \ll k^2, l^2$. The zonal (x) component of planetary Rossby waves always propagate from east to west, while the topographic Rossby waves in the examples shown here propagate with shallow-water on their right. The group velocity and the energy propagation generally depends on the wave number, but can be in either direction.

A.5 Rossby Adjustment

The derivation of the equations describing the end state in the case of Rossby adjustment takes a different path. The linearized basic shallow-water equations read

$$\frac{\partial U}{\partial t} - fV = -gH\frac{\partial \eta}{\partial x}, \tag{A.30}$$

$$\frac{\partial V}{\partial t} + fU = -gH\frac{\partial \eta}{\partial y}, \tag{A.31}$$

$$\frac{\partial \eta}{\partial t} + \frac{\partial U}{\partial x} + \frac{\partial V}{\partial y} = 0. \tag{A.32}$$

Here, $(U,V) = (hu,hv)$ is the volume transport. To simplify the derivation we assume that the depth is constant.

We aim to find a single equation for η, and take the divergence of (A.30) and (A.31), and the time derivative of (A.32). We can then eliminate U and V and obtain

$$\frac{\partial^2 \eta}{\partial t^2} + \nabla\cdot\left(c_0^2\nabla\eta\right) + Hf\zeta = 0, \tag{A.33}$$

in which $c_0^2 = gH$. An equation for the vorticity can be obtained by taking the curl of (A.30) and (A.31), and combining with the continuity equation (A.32):

$$H\frac{\partial \zeta}{\partial t} - f\frac{\partial \eta}{\partial t} = 0. \tag{A.34}$$

Using (A.34) to eliminate ζ in (A.33), we obtain (see also [35], Eq. 3.6.9, p. 69)

$$\frac{\partial}{\partial t}\left[\left(\frac{\partial^2}{\partial t^2}+f^2\right)-\nabla\cdot\left(c_0^2\nabla\eta\right)\right]=0. \tag{A.35}$$

It is straightforward to integrate this equation in time, and assuming zero initial velocities and that $\eta=\eta_0$, we have

$$\frac{\partial^2\eta}{\partial t^2}-c_0^2\nabla^2\eta+f^2(\eta-\eta_0)=0. \tag{A.36}$$

The transient solution to this equation describes long surface waves modified by rotation, usually referred to as Poincaré waves. The steady solution $\bar{\eta}$ is the result of adjustment to the local rotation as a permanent modification of the mean surface level with velocities in geostrophic balance. This process is referred to as Rossby adjustment. The steady state is found by solving the Klein-Gordon equation that results from removing the time dependence in (A.36):

$$-c_0^2\nabla^2\bar{\eta}+f^2(\bar{\eta}-\eta_0)=0. \tag{A.37}$$

The length scale given by $L_R=c_0/f$ is the Rossby radius of deformation, within which a disturbance will be trapped by rotation and the steady-state solution will be dominated by a geostrophic balance.

References

[1] R. Asselin. Frequency filter for time integrations. *Monthly Weather Review*, 100(6):487–490, 1972.

[2] W. Blumen. Geostrophic adjustment. *Reviews of Geophysics*, 10(2):485–528, 1972.

[3] A. R. Brodtkorb, H. H. Holm, and M. L. Sætra. Comparing performance and usability of CUDA and OpenCL with Python. In review, 2019.

[4] A. R. Brodtkorb and M. L. Sætra. Explicit shallow water simulations on GPUs: Guidelines and best practices. In *XIX International Conference on Water Resources, CMWR 2012, June 17–22, 2012*. University of Illinois at Urbana-Champaign, 2012.

[5] A. R. Brodtkorb, M. L. Sætra, and M. Altinakar. Efficient shallow water simulations on GPUs: Implementation, visualization, verification, and validation. *Computers & Fluids*, 55(0):1–12, 2012.

[6] A. Chertock, M. Dudzinski, A. Kurganov, and M. Lukáčová-Medvid'ová. Well-balanced schemes for the shallow water equations with coriolis forces. *Numerische Mathematik*, Dec 2017.

[7] B. Cockburn, G. E. Karniadakis, and C.-W. Shu. The development of discontinuous galerkin methods. In B. Cockburn, G. E. Karniadakis, and C.-W. Shu, editors, *Discontinuous Galerkin Methods*, pages 3–50, Berlin, Heidelberg, 2000. Springer Berlin Heidelberg.

[8] R. Comblen, J. Lambrechts, J.-F. Remacle, and V. Legat. Practical evaluation of five partly discontinuous finite element pairs for the non-conservative shallow water equations. *International Journal for Numerical Methods in Fluids*, 63(6):701–724, 2010.

[9] H. C. Davies. A lateral boundary formulation for multi-level prediction models. *Quarterly Journal of the Royal Meteorological Society*, 102(432):405–418, 1976.

[10] M. de la Asunción, J. Mantas, and M. Castro. Simulation of one-layer shallow water systems on multicore and CUDA architectures. *The Journal of Supercomputing*, 58(2):206–214, Nov 2011.

[11] O. Delestre, C. Lucas, P.-A. Ksinant, F. Darboux, C. Laguerre, T.-N.-T. Vo, F. James, and S. Cordier. SWASHES: a compilation of shallow water analytic solutions for hydraulic and environmental studies. *International Journal for Numerical Methods in Fluids*, 72(3):269–300, 2013.

[12] S. Frazão, F. Alcrudo, and N. Goutal. Dam-break test cases summary. In *The Proceedings of the 4th CADAM meeting*, 1999.

[13] S. Frazão, X. Sillen, and Y. Zech. Dam-break flow through sharp bends, physical model and 2D Boltzmann model validation. In *The Proceedings of the 1st CADAM meeting*, 1998.

[14] J. Galewsky, R. K. Scott, and L. M. Polvani. An initial-value problem for testing numerical models of the global shallow-water equations. *Tellus A: Dynamic Meteorology and Oceanography*, 56(5):429–440, 2004.

[15] A. E. Gill. *Atmosphere-Ocean Dynamics*. International Geophysics. Academic Press, 1982.

[16] S. Gottlieb, C.-W. Shu, and E. Tadmor. Strong stability-preserving high-order time discretization methods. *SIAM Review*, 43(1):89–112, 2001.

[17] N. Goutal. The Malpasset dam failure, an overview and test case definition. In *The Proceedings of the 4th CADAM meeting*, 1999.

[18] N. Goutal and F. Maurel. Proceedings of the 2nd Workshop on Dam-Break Wave Simulation. Technical report, Groupe Hydraulique Fluviale, Département Laboratoire National d'Hydraulique, Electricité de France, 1997.

[19] R. Grotjahn and J. J. O'Brien. Some inaccuracies in finite differencing hyperbolic equations.

Monthly Weather Review, 104(2):180–194, 1976.

[20] J.-M. Hervouet and A. Petitjean. Malpasset dam-break revisited with two-dimensional computations. *Journal of Hydraulic Research*, 37:777–788, 1999.

[21] H. H. Holm, A. R. Brodtkorb, M. L. Sætra, G. Broström, and K. H. Christensen. Supplementary material to evaluation of selected finite-difference and finite-volume approaches to rotational shallow-water flow. `https://doi.org/10.5281/zenodo.3204200`, 5 2019.

[22] C. Huxley and B. Syme. TUFLOW GPU-best practice advice for hydrologic and hydraulic model simulations. In *37th Hydrology & Water Resources Symposium 2016: Water, Infrastructure and the Environment*, pages 195–203. Engineers Australia, 2016.

[23] A. Kurganov and G. Petrova. A second-order well-balanced positivity preserving central-upwind scheme for the Saint-Venant system. *Communications in Mathematical Sciences*, 5:133–160, 2007.

[24] M. Lastra, J. Mantas, C. Urea, M. Castro, and J. Garca-Rodrguez. Simulation of shallow-water systems using graphics processing units. *Mathematics and Computers in Simulation*, 80(3):598–618, 2009.

[25] R. LeVeque. *Finite Volume Methods for Hyperbolic Problems*. Cambridge University Press, 2002.

[26] W.-Y. Liang, T.-J. Hsieh, M. Satria, Y.-L. Chang, J.-P. Fang, C.-C. Chen, and C.-C. Han. A GPU-based simulation of tsunami propagation and inundation. In *Algorithms and Architectures for Parallel Processing*, volume 5574 of *Lecture Notes in Computer Science*, pages 593–603, Berlin/Heidelberg, 2009. Springer Verlag.

[27] K. T. Mandli, A. J. Ahmadia, M. Berger, D. Calhoun, D. L. George, Y. Hadjimichael, D. I. Ketcheson, G. I. Lemoine, and R. J. LeVeque. Clawpack: building an open source ecosystem for solving hyperbolic pdes. *PeerJ Computer Science*, 2:e68, 2016.

[28] P. Marchesiello, J. C. McWilliams, and A. Shchepetkin. Open boundary conditions for long-term integration of regional oceanic models. *Ocean Modelling*, 3(1):1–20, 2001.

[29] E. A. Martinsen and H. Engedahl. Implementation and testing of a lateral boundary scheme as an open boundary condition in a barotropic ocean model. *Coastal Engineering*, 11(5):603–627, 1987.

[30] L. R. Mendez-Nunez and J. J. Carroll. Comparison of Leapfrog, Smolarkiewicz, and MacCormack Schemes Applied to Nonlinear Equations. *Monthly Weather Review*, 121(2):565–578, 1993.

[31] F. Mesinger and A. Arakawa. *Numerical Methods Used in Atmospheric Models*, volume 1 of *GARP publications series*. World Meteorological Organization, International Council of Scientific Unions, 1976.

[32] MIKE Powered by DHI. MIKE 21 graphical processing units (GPU) benchmarking report. Technical report, DHI, 2019. `https://www.mikepoweredbydhi.com/-/media/shared%20content/mike%20by%20dhi/flyers%20and%20pdf/product-documentation/gpu-benchmarking-report.pdf`, accessed: 2019-05-21.

[33] R. D. Nair, S. J. Thomas, and R. D. Loft. A discontinuous galerkin global shallow water model. *Monthly Weather Review*, 133(4):876–888, 2005.

[34] S. Noelle, N. Pankratz, G. Puppo, and J. R. Natvig. Well-balanced finite volume schemes of arbitrary order of accuracy for shallow water flows. *Journal of Computational Physics*, 213(2):474–499, 2006.

[35] J. Pedlosky. *Geophysical Fluid Dynamics*. Springer New York, 1987.

[36] N. A. Phillips. An example of non-linear computational instability. *The Atmosphere and the Sea in motion*, 501, 1959.

[37] X. Qin, R. J. LeVeque, and M. R. Motley. Accelerating wave-propagation algorithms with

adaptive mesh refinement using the graphics processing unit (GPU). *CoRR*, abs/1808.02638, 2018.

[38] A. J. Robert, F. G. Shuman, and J. P. Gerrity. On partial difference equations in mathematical physics. *Monthly Weather Review*, 98(1):1–6, 1970.

[39] L. P. Røed. Documentation of simple ocean models for use in ensemble predictions. Part I: Theory. Technical report, Norwegian Meteorological Institute, 2012.

[40] L. P. Røed. *Atmospheres and Oceans on Computers*. Springer International Publishing, 2018.

[41] A. F. Shchepetkin and J. C. McWilliams. The regional oceanic modeling system (ROMS): a split-explicit, free-surface, topography-following-coordinate oceanic model. *Ocean Modelling*, 9(4):347–404, 2005.

[42] A. Sielecki. An energy-conserving difference scheme for the storm surge equations. *Monthly Weather Review*, 96(3):150–156, 1968.

[43] W. Thacker. Some exact solutions to the nonlinear shallow-water wave equations. *Journal of Fluid Mechanics*, 107:499–508, 1981.

[44] E. Toro. *Shock-Capturing Methods for Free-Surface Shallow Flows*. John Wiley & Sons, Ltd., 2001.

[45] G. Tumolo, L. Bonaventura, and M. Restelli. A semi-implicit, semi-lagrangian, p-adaptive discontinuous galerkin method for the shallow water equations. *Journal of Computational Physics*, 232(1):46–67, 2013.

[46] A. Valiani, V. Caleffi, and A. Zanni. Case study: Malpasset dam-break simulation using a two-dimensional finite volume method. *Journal of Hydraulic Engineering*, 128:460–472, 2002.

[47] D. L. Williamson, J. B. Drake, J. J. Hack, R. Jakob, and P. N. Swarztrauber. A standard test set for numerical approximations to the shallow water equations in spherical geometry. *Journal of Computational Physics*, 102(1):211–224, 1992.

[48] J. G. Zhou. *Lattice Boltzmann Methods for Shallow Water Flows*. Springer-Verlag Berlin Heidelberg, 2004.